268

The impact of increased boundary layer vertical resolution on the ECMWF forecast system

J. Teixeira

Research Department

February 1999

1. INTRODUCTION

Adequate vertical resolution in the lower troposphere of global atmospheric models is important for the proper representation and prediction of boundary layer processes. It has been known for a long time that a good representation of the atmospheric boundary layer is fundamental to achieve realistic weather forecasts and climate predictions. Furthermore, boundary layer processes are among the most important atmospheric phenomena in terms of its impact on human activities. The atmospheric boundary layer also has a strong role in determining the air-sea fluxes and as a consequence is very important for seasonal forecasting.

There are some studies dedicated to the analysis of the role of vertical resolution in global atmospheric models in general (*Simmons*, 1979, 1991; *Lindzen and Fox-Rabinovitz*, 1989; *Kitoh and Tokioka*,1986; *Williamson and Olson*, 1998; *Williamson et al.*, 1998). *Lindzen and Fox-Rabinovitz* (1989) discuss the consistency between horizontal and vertical resolution. But it is not clear to what extent their approach applies to forecast-assimilation systems. Some of the recent studies of vertical resolution in global models are specifically about stratospheric resolution (*Boville and Randel*, 1992; *Simmons*, 1994). At ECMWF the impact of increased stratospheric vertical resolution upon the assimilation and forecast system is being studied (*Untch et al.*, 1996).

The effect of vertical resolution and boundary layer processes in the context of global models has been the subject of several recent papers. *Beljaars* (1991) studied the impact of increased resolution upon a simple one-dimensional Ekman model. *Delage* (1988) considered the position of the lowest levels in the boundary layer of global atmospheric models. *Gregory et al.* (1998a) examined the interaction between the convection and the turbulence parametrizations due to increased vertical resolution. More specifically *Raisannen* (1996) discussed the effect of increased vertical resolution on clear-sky radiation calculations. There are however several vertical resolution sensitivity studies with high resolution (of the order of 20 m) one-dimensional boundary layer models. *Van Meijgaard and Van Ulden* (1998) and *Lenderink and Holtslag* (1998), for example, studied the impact of vertical resolution in simulations of stratocumulus.

Here a detailed study of the performance of a new enhanced vertical resolution configuration of 40 levels, compared to the current operational configuration of 31 levels is presented. This analysis will focus on the quality of the cloudy boundary layer simulations and on the realism of the forecast climate. Subjects like the low level wind structure and the overall behaviour of the forecast-assimilation system are also discussed.

In section 2 a discussion about the vertical configuration of the ECMWF model is presented. Section 3 gives results of simulations of ASTEX Lagrangian 1, using the one-column model. A comparison, against global observations, of the performances of both configurations in long integrations (120 days) is shown in section 4. A discussion of the quality of the high resolution simulations in the context of data assimilation experiments is presented in section 5, with conclusions in section 6.

2. The configuration

In global atmospheric models the vertical resolution is usually not uniform. In the ECMWF model the finest resolution, in height, is near the surface and degrades upwards. In pressure the resolution is highest close to the

surface and degrades upwards until some level in the troposphere. Above that, the resolution increases again until the 100 hPa level where it reaches a value of 20 hPa that is constant up to the top of the model.

Apart from these characteristics there are few constraints on where to increase the resolution. However, contrary to many computational fluid dynamics applications a simple study of the physics of the problem does not determine where to have higher resolution. In fact, in the ECMWF model there are 6 prognostic variables that can have sharp gradients at several different heights. Moreover, adaptive grid methods are not easily feasible, not only because of computational cost but also because it is not clear which physical quantities should be minimized.

Consider the example of a thick stratocumulus deck over the sea. The shape of the temperature and moisture profiles suggests that, close to the inversion, higher resolution is needed in order to resolve better the sharp gradients. On the other hand the wind speed does not necessarily experience a major change through the inversion but always has a strong gradient close to the surface. In this case high resolution would be needed near the surface and close to the inversion. Duynkerke and Driedonks (1987), for example, use a one-dimensional boundary layer model to simulate stratocumulus, with a vertical resolution that is actually higher close to the surface and close to the inversion. If the inversion rises this creates a problem: either the model has an adaptive grid or the high resolution is not where it is most needed. In a global model the problem is even more complicated since the inversion can be at a different heights depending on the geographical location.

Paradoxically some phenomena like fog which are usually assumed to be realistically simulated only with very high resolution close to the surface (e.g. Welch et al. 1985) are actually reasonably well modelled with the current operational (L31) ECMWF vertical resolution (Teixeira 1997). However, the resolution close to the surface (30m and 150m for the two lowest model levels) is still far from ideal.

Another problem is the fact that the different parametrization schemes suffer from different problems and require high resolution at different heights of the atmosphere. Close to the cloud top there is a strong longwave radiative cooling. This cooling is usually distributed in a very thin vertical layer of around 20m to 50m (e.g. Stull 1989) from the cloud top downwards. The shortwave radiation on the other hand has impact in a deeper layer inside the cloud.

In order to investigate if the current longwave radiation parametrization is capable of handling an increase in vertical resolution, a simple experiment with the radiation code alone was performed: the vertical resolution was initially set to 80 hPa thickness in pressure for every level. A cloud was located between 820 hPa and 900 hPa. As can be seen in fig.1 the longwave radiation cooling is concentrated in the cloud layer and distributed evenly in that layer. When the vertical resolution is increased by 10 times (to a pressure thickness of 8 hPa) the longwave cooling is concentrated in a thin layer close to the top of the cloud and the warming is concentrated on a thin layer close to the bottom of the cloud. This example shows that the longwave parametrization behaves correctly and converges to a realistic solution when the vertical resolution is increased.

However, the other parametrizations do not necessarily respond well to the more realistic forcing of the longwave cooling. In reality the atmosphere responds to the cooling at the cloud top by generating circulations, either only

inside the cloud (decoupled case) or throughout the entire boundary layer down to the surface. Cloud top cooling is the main cause for turbulent mixing in the stratocumulus capped boundary layer.

To achieve a proper simulation of this process, the sub-grid scale mixing parametrizations would have to respond to differential cooling (at cloud top) and warming (at cloud bottom) with a realistic mixing inside the cloud. However, the model's vertical diffusion parametrization scheme is not able to respond directly to this differential cooling caused by radiation. On the other hand, the shallow convection scheme is vertical resolution dependent and is not necessarily prepared to respond realistically to the enhanced vertical resolution.

Two different configurations of enhanced vertical resolution were tried: 39 and 40 levels (L39 and L40). The model-layer pressure thickness and the corresponding pressure of the model level are shown in fig. 2 for the enhanced vertical resolution configurations and the operational model. As mentioned in the beginning of this section the operational L31 resolution, in terms of pressure thickness, is highest close to the surface and degrades upwards until around 730 hPa where it reaches a value of about 46 hPa. Above that, the resolution increases again until the 100 hPa level where it reaches 20 hPa that remains constant up to the top of the model.

The two new vertical configurations, L39 and L40, reproduce this general behaviour. The main differences between these new versions and the operational L31 model are that the resolution is everywhere, from the surface to the 100 hPa level, higher than the L31 resolution and the worst resolution is now at about 575 hPa where it reaches a value of around 38 hPa. In general the resolution is significantly increased in the boundary layer when compared with the operational model.

The main difference between the two new configurations is that the height of the lowest model level of the L40 configuration is at about 10 m above the surface while the L39 lowest model level height is the operational value of about 33 m. Looking in detail to the first levels above the surface it can be seen that the L40 configuration has a more gradual increase of layer thickness with height than the L39 configuration.

Some experimentation has been carried out with the L39 version, but the L40 configuration has obvious advantages: it has better resolved surface stable layers, direct 10 m wind output for application over the ocean and a more natural distribution of levels near the surface. Therefore, only results with the L40 model will be presented in this paper.

The distribution in height of the L40 and L31 model-layer height thicknesses, for the first 1500 m above the surface, is shown in fig. 3. It can be seen that the L40 model has twice the number of levels (12 levels) in the first 1500 m than the L31 version. In general the L40 version doubles the vertical resolution compared to the L31 model. The distribution of full model levels for the L31 and L40 configurations is shown in fig. 4.

In global atmospheric models the vertical turbulent mixing is usually parametrized using a k-diffusion approach. This parametrization creates a system of non-linear diffusion equations with numerical stability problems (e.g. *Girard and Delage*, 1990; *Beljaars* 1991). This stability problems are somehow "controlled" in the operational L31 version by using a "more-than-implicit" scheme (*Beljaars*, 1991) to integrate the vertical diffusion equation. A good diagnostic of potential stability problems with a higher resolution model can be provided by the parameter

$\alpha = k\Delta t / \Delta z^2$, where k is the vertical diffusion coefficient, Δt is the time step and Δz is the vertical grid length. The bigger the α the more potentially unstable the vertical diffusion scheme is. It can be easily seen that if the resolution is increased, like at the lowest model level, from around 33 m to 10 m, parameter α increases by an order of magnitude. However, from the experimentation carried out, the L40 model does not seem to introduce significant additional numerical problems.

3. The One-Column model and ASTEX Lagrangian 1

Before considering experimentation on the ECMWF global model, the new resolution was tested in the one-column (1C) framework. The 1C version of CY15R6 of the ECMWF model was used to simulate ASTEX Lagrangian 1.

The ASTEX observational programme was carried out from 1- 28 of June, 1992, from a base located on the islands of Santa Maria and Porto Santo. ASTEX was designed to study stratocumulus and the transition to trade cumulus. The ASTEX Lagrangians (*Bretherton and Pincus*, 1995) were two particular observation periods where the trajectory of a column of air within the boundary layer was followed for some time. ASTEX Lagrangian1 corresponds to a period where the trajectory was followed for 42 hours. The experiment started at 16 UTC on 12 June 1992, during which the boundary layer advected 1400 km from (41°N, 24°W) to (29°N, 29°W). The sea-surface temperature (SST) increased from 290 to 294 K, with a particularly rapid rise between 00 and 12 UTC on June 13 (hours 8 to 20 of the simulation period). The cloud changed from an initial solid well-mixed stratocumulus layer to a 160 hPa thick layer filled mainly with cumuli.

The setup of the 1C model for the ASTEX Lagrangian 1 is the following: vertical resolution of 31 and 40 levels; time-step of 900 s; semi-Lagrangian vertical advection; the surface pressure is kept constant in time with a value of 1019 hPa; initial values of u, v, T, q, a and l derived from the ASTEX observations; the values of ω, Ug and Vg are changing in time according to the ASTEX observations; the SST, latitude and longitude are also changing in time according to the ASTEX data, providing the Lagrangian nature to the 1C simulation.

In fig. 5 the hourly observations of the liquid water profile are shown. These observations are in a 10 hPa grid resolution. The transition regime from stratocumulus to cumulus is evident, with an initial solid stratocumulus deck just above 1000 hPa. The liquid water content peaked between hours 12 and 18 with a value of around 0.5 g/kg. Although the boundary layer is steadily growing since hour 3, between hour 21 and 24 it gets deeper and a trade wind type of boundary layer starts to be evident by the end of the simulation, when the boundary layer top is at 850 hPa and the liquid water content is between 0.1 and 0.2 g/kg. This transition is also clear in the relative humidity structure (fig. 6) where the initially shallow (top at 960 hPa) and moist boundary layer (the average relative humidity is above 95% until around hour 18) is followed by the boundary layer growth that ends in a deeper (top at around 850 hPa) boundary layer with a drier sub-cloud layer with a relative humidity lower than 90%.

Figure 7 shows the simulated hourly mean liquid water at different levels produced by the L31 model. Comparing fig. 7 with fig. 5 it shows that the results are reasonable, with the simulation of a transition from a low level

stratified cloud to a shallow cumulus situation, together with the corresponding deepening of the boundary layer. The main problem is that after 21 hours of simulation the model liquid water becomes almost negligible. This does not happen with the cloud fraction (not shown) that keeps being close to 1 until a few hours before the end of ASTEX Lagrangian 1.

The peak values of liquid water content in the stratified cloud are above 0.4 g/kg which is close to the observations, however the period when this peak values occur is before the observed one (between hour 9 and 15 in the model). The simulated stratified cloud is just one model level thick (level 29) while in the observations the boundary layer has been growing from the start of the simulation. Even when the observations are interpolated to the model grid (not shown) the cloud is more than one level thick and its peak values are at level 28. After hour 21, and in spite of the lack of liquid water, the boundary layer starts to get deeper and by the end of the simulation period it reaches around 850 hPa as in the observations. However, the model liquid water content is far too big: it reaches values larger than 0.3 g/kg. It should be stressed that the deepening of the boundary layer is realistic, which can also be confirmed with plots of the model relative humidity (not shown).

A previous simulation of ASTEX Lagrangian 1 with the 1C model (Teixeira et al., 1996) has shown that doubling the boundary layer vertical resolution improves the results. To test the sensitivity of the 1C model to an increase in boundary layer resolution in a more consistent manner, the ASTEX Lagrangian 1 simulation is performed with the L40 configuration. In fig. 8 the model results for the hourly mean liquid water are shown. By analysing the previous figures it can be seen that the results with the L40 configuration are in some aspects better than with the L31 resolution. In particular between hour 21 and 33 the liquid water does not disappear in the L40 version, like it does during the L31 simulation. This is related to the fact that shallow convection, which is the main liquid water source in the second half of the simulation, is more intense, more frequent and is triggered earlier with the increased vertical resolution. With a better vertical resolution the convection algorithm "detects" instability in shallower layers than before. Also, the shallow convection scheme only becomes active when convection covers at least two model levels and therefore the scheme handles the shallower clouds better at high resolution.

The liquid water values in the stratocumulus region (0.5 g/kg) are good when compared with the observations and better than the L31 values. The results with the L40 resolution are worse than with L31 in two particular aspects: (i) the amount of liquid water during the final period of the simulation is far too high when compared with the observations and the L31 version and (ii) the boundary layer becomes too deep in the shallow cumuli region (about 50 hPa deeper than the L31 model).

3.1 Sources and sinks of liquid water.

One of the main problems of the ECMWF model's cloud simulations is the underestimation of stratocumulus (*Teixeira*, 1997; *Jakob*, 1998) and the lack of liquid water in fig. 7 after 21 hours of simulation is probably an example of it. In order to understand why the L31 version is losing more liquid water than the L40 model a more detailed analysis of the liquid water sources and sinks is performed. In figures 9(a) to 9(d) the evolution of the following terms of the liquid water equation for the L31 model are shown: the production of liquid water due to detrainment from convection, the production of liquid water due to large-scale condensation, the destruction of liquid water due to large-scale evaporation and the destruction of liquid water due to the conversion of water into

rain. The units are in g/kg/day. Of all the source and sink terms in the liquid water equation, these four terms are for this situation the most important ones.

Analysing the figures it can be seen that during the stratocumulus period the two dominant terms are: a positive tendency from the large-scale condensation and a negative tendency from the conversion of water into rain. During the transition period the positive dominant term is detrainment from convection and the negative tendency is mainly due to the large-scale evaporation. On the final stages the production of liquid water is due to the detrainment and the destruction is shared between large-scale evaporation and conversion into rain. When the liquid water disappears in the L31 version, just after going one level up, around hour 24, the two dominant processes are detrainment and evaporation. Although it is not very clear from these figures, what happens is that the evaporation is higher than the detrainment which leads to the decrease of liquid water.

This can be more clearly investigated by analysing fig. 10 where the liquid water evolution at level 28 (in 10^{-1}g/kg), the total liquid water tendency and the detrainment and evaporation tendencies (all in g/kg/day) are shown. Since there is no vertical mixing of liquid water, the cloud can only go one level up when there is a positive source at the level above. The detrainment that starts at about hour 22 creates a positive liquid water tendency that will last up to about hour 24 when the evaporation becomes higher than the detrainment. During about an hour the evaporation will be clearly higher than the detrainment which will reduce the liquid water to half of its previous value (from 0.1 to 0.05 g/kg). From hour 25 onwards, the evaporation is slightly higher than the detrainment creating a continuous negative tendency.

Figures 11(a) to 11(d) show the evolution of the following terms of the liquid water equation for the L40 model: production of liquid water due to detrainment and large-scale condensation and destruction of liquid water due to large-scale evaporation and precipitation (all in g/kg/day). The role of the different terms is similar to the L31 version during the three main stages of the simulation: the stratocumulus, the transition and the shallow cumulus periods. One major difference is that the absolute values of all the tendencies are larger in the L40 version. Detrainment and evaporation more than double in certain circumstances, particularly in the transition period. In general, the tendency terms are more noisy in the L40 version, particularly detrainment. The detrainment term is larger because shallow convection is more frequent and intense in the L40 version. The more intense convection is also believed to be the main factor behind the increase in the large-scale evaporation term, through cumulus induced subsidence. The large-scale condensation is increased because the longwave cooling near the cloud top increases in the L40. The conversion of water into rain is larger throughout the simulation, which is due to the higher values of liquid water content in the L40 version.

The major difference between the two simulations is that the liquid water does not disappear in the L40 version. The reason for this is that in the L40 model the detrainment is in general higher than the evaporation during the transition period. This is not very clear from the figures shown but can be confirmed by an analysis of the times series of these terms at different vertical levels (not shown). Convection, and consequently detrainment of liquid water, starts in the L31 version after hour 21, while in the L40 version it starts after hour 12. This confirms that the higher resolution version is able to trigger the convection scheme earlier and more frequently than the L31 version.

3.2 Liquid water path and cloud fraction.

In fig. 12 the evolution of the Liquid Water Path (LWP) for the observations, the L31 model and the L40 model is shown. The simulated LWP during the first 10 hours is realistic for both models. After that, both models underestimate the observed peak values of around 160 g/m^2, but the L40 LWP evolution is reasonable when compared to the observations until around hour 24. After hour 16 the observed LWP decreases to values between 50 to 70 g/m^2 and the two models behave rather differently: the L40 LWP increases while the LWP from the L31 version decreases until it reaches values close to 0 g/m^2. After hour 28 and until the end of the simulation the observations show values of LWP between 40 to 60 g/m^2. During this period the LWP from both model versions reaches values that are clearly too high.

The L40 underestimates the observed LWP between hour 12 and 18. This has to do with the fact that in the model the stratocumulus is basically just one model level thick. This is in sharp contrast with the observations which when interpolated to the L40 grid are 3 to 4 levels thick. The observations also show a much more vertically dynamic stratocumulus, with the cloud growing upwards and downwards during the ASTEX Lagrangian. This is problematic for the model since: i) the boundary layer cloud part of the cloud scheme can only generate clouds that are one level thick (see *Tiedtke* 1993); ii) the cloud top entrainment mechanism is not efficient in mixing the cloud vertically and there is no other process to mix the cloud in the vertical; and iii) there is a potential positive feedback between the large-scale condensation term and the longwave cooling which tends to concentrate the cloud in just one level.

The knowledge of the observed cloud amount structure is limited when compared with the information available for the liquid water. The observed boundary layer cloud cover is around 100% throughout most of the simulation until some hours before the end when it drops to about 70%. Both models give a general picture of the time evolution of cloud fraction that is very similar. In the L31 model there is no drop in cloud fraction as there is in the liquid water. The main differences are in the last part of the simulation. The cloud of the L40 model is far too deep when compared with the observations or the L31 model (as can be inferred from the figures that show the liquid water evolution).

The cloud fraction structure in the vertical is also different between the two models. In fig. 13 the cloud fraction at the end of the simulation period, for both models and the observations from *DeRoode and Duynkerke* (1997), versus a normalized height, is shown. The height is normalized between the cloud base and cloud top. In the model the cloud base height is chosen as the height of the vertical level below the first level (going from the surface upwards) to have a cloud fraction higher than 5%. The cloud top height is chosen to be the height of the level above the last level to have a cloud fraction above 5%. Fig. 13 shows that the vertical structure of the L40 cloud fraction is much closer to the observations. In the L31 model the peak value of cloud fraction is below the middle of the cloud, and decreases above that, while in the L40 model and in the observations the cloud fraction increases in a similar manner from the cloud base to the cloud top. The L40 model reaches the peak value not far from the observations peak value (close to the cloud top).

In terms of relative humidity (not shown) both models produce a reasonable simulation with the boundary layer growth and the transition from a shallower and moister to a deeper and drier boundary layer. In general, the transition regime from stratocumulus to cumulus clouds is better captured with the increased resolution. The

reason is that the shallow convection scheme, which is in the model responsible for the realistic transition from stratocumulus to trade cumulus, is more active at high resolution. However, the shallow convection scheme is eroding the inversion too quickly, probably as the result of a too strong interaction with radiation, generating a boundary layer that is too deep in the L40 model. In section 5 a comparison between radiosondes and model (L31 and L40) forecasts will allow to analyse in detail the quality of the inversion height simulations at high resolution.

4. Long integrations

Long integrations (120 days) with the 31 levels and the 40 levels versions, of the IFS cycle 15R6, were performed for the periods of November-December-January-February 1986/1987 and May-June-July-August 1987. To analyse the quality of the results some diagnostics were performed which compared model data against satellite data and surface climatology. The analysis is restricted to the last 90 days of each period. Only results of the June-July-August (JJA) period will be analysed in detail, since the same conclusions can be drawn from the analysis of December-January-February (DJF) period.

4.1 Comparison with observations

4.1.1 Cloud cover and ISCCP

Figure 14(a) shows the global distribution of the mean cloud cover according to the International Satellite Cloud Climatology Project (ISCCP) for the period JJA 1987. For more details about ISCCP the reader is referred to Rossow and Schiffer (1991) and references therein. Figures 14(b) and 14(c) show, respectively, the differences between the L31 mean cloud cover and ISCCP and the L40 mean cloud cover and the ISCCP data, for the same period.

It can be seen that the cloud cover in the L40 configuration has in general increased when compared with the L31 model and that this clearly improves the representation of clouds when compared with the L31 resolution and the satellite observations. This is clear all over the globe but particularly over the stratocumulus areas, the southern ocean and in general over the sub-tropical and extra-tropical regions. In some parts of the stratocumulus and the southern ocean areas the cloud cover improves by up to 50% with the higher vertical resolution.

The rise in total cloud cover is mainly due to the increase of low clouds. Taking into account the analysis performed with the ASTEX Lagrangian 1 case, this can probably be explained by an increase of the cloud fraction and liquid water production due to large scale condensation and detrainment from convection. The increase of cloud cover in the trades is a clear indicator of an increase in the shallow convection activity due to the higher vertical resolution.

4.1.2 Outgoing Longwave Radiation and ERBE

Figure 15(a) shows the global distribution of Outgoing Longwave Radiation (OLR) as estimated by the Earth Radiation Budget Experiment (ERBE) for the period JJA 87. ERBE is described in detail in Barkstrom and Smith (1986). Figures 15(b) and 15(c) show respectively the OLR differences between the L31 model and ERBE and between the L40 model and ERBE.

The increase of clouds with resolution is reflected in a positive way in the OLR results. In fact, the previous figures show that the model errors in OLR are in general less with the new vertical resolution. In fig. 15(a) the OLR has a negative sign, which implies that if, for example, the model has a positive bias, this means that the equivalent temperature at which the column of the atmosphere is radiating in the model is smaller than the equivalent observed temperature.

In the tropical regions over the oceans the model has a positive OLR bias. With the high vertical resolution this bias is substantially decreased. Changes in the OLR are often difficult to interpret and they can be related, among other things, to changes in the cloud amount but also with the variability and frequency of occurrence of convection and clouds. The negative OLR bias that is globally spread in the L31 model is reduced by the L40 version. This is particularly true in areas like North America, Russia and Central Africa. The general increase in cloud cover with the L40 version is probably the reason behind the improvement of the L31 OLR negative bias.

4.1.3   Top Shortwave Radiation and ERBE

Figure 16(a) shows the global distribution of Top Shortwave Radiation (TSR) as measured by ERBE for the period JJA 87. Figures 16(b) and 16(c) show respectively the TSR differences between the L31 model and ERBE and between the L40 model and ERBE.

In the stratocumulus areas the increase of clouds with the L40 resolution is in better agreement with the observations from ERBE. In fact the positive bias of the L31 model in these regions is reduced with the new resolution by as much as 15 to 30 W/m^2. In general the increase of low cloud amounts in the L40 version generates a decrease in the positive bias of TSR all around the globe. The L31 model negative bias of TSR (overestimation of albedo) becomes slightly worse with the L40 model in some areas and slightly better in other areas, but in most places remains unchanged.

4.1.4   Precipitation and GPCP

Figure 17(a) shows the global distribution of precipitation (mm/day) as estimated by the Global Precipitation Climatology Project (GPCP) for the period JJA 87. More details about GPCP can be found in Huffman et al. (1997). Figures 17(b) and 17(c) show respectively the precipitation differences between the L31 model and GPCP and between the L40 model and GPCP.

From the analysis of the figures it is obvious that the L40 model makes a much improved simulation of precipitation in the equatorial regions. In the ITCZ over the Pacific and the Atlantic the L40 model reduces significantly the positive bias compared to the L31 model. In some areas the error is reduced by more than 8 mm/day (in a total error of up to 16 mm/day in the L31 model). Also over the West Pacific the L31 error is reduced. Over the monsoon region the L40 results are also better and over Central America the L31 negative bias is also reduced. The ITCZ area is also broader in the L40 model which is closer to what is observed.

4.2 Comparison with surface climatology

For seasonal forecasting (*Anderson et al.*, 1997), ECMWF uses a coupled ocean-atmosphere system to produce 6 month forecasts. One of the major problems of such a system is the sea surface temperature drift (*Stockdale et al.*, 1997), which is related to defficiencies in the surface fluxes produced by the atmospheric model. In this

section an assessment is made of the quality of the surface fluxes generated by the L40 and the L31 versions of the ECMWF global atmospheric model. To make this analysis the model results are compared with a climatology of surface fluxes. It has to be stressed that comparisons against a climatology are less reliable than the comparisons against observations that were performed in section 4.1 because of the non-negligible annual variability and of shortcomings of the data.

4.2.1 Surface Latent Heat Flux

Figure 18(a) shows the global distribution of the Surface Latent Heat Flux (SLHF) as given by the climatology of *Silva et al.* (1994) for JJA. This climatology is based on individual observations that are part of the Comprehensive Ocean-Atmosphere Data Set (COADS) from January 1945 to December 1989. Negative values in the surface fluxes correspond to heat being transferred from the ocean to the atmosphere which leads to a cooling of the ocean surface. Positive values correspond to a warming of the ocean surface. Figures 18(b) and 18(c) show respectively the SLHF differences between the L31 model and the climatology and the L40 model and the climatology.

From the figures it can be seen that the results for both versions of the model are fairly similar. In some areas, like the Bay of Bengal or off the East coast of Australia, there are significant improvements with the L40 version. An excessive cooling of the surface of the ocean, in these areas, produced by the L31 model is reduced by the higher resolution version. The SLHF in the stratocumulus areas off North and South America is also more realistic with the L40 model leading to a significant reduction of the positive SLHF bias in those areas.

4.2.2 Surface Shortwave Radiation

Figure 19(a) shows the global distribution of Surface Shortwave Radiation (SSR) as given by the climatology of *Silva et al* (1994) for JJA. Figures 19(b) and 19(c) show respectively the SSR differences between the L31 model and climatology and the L40 model and the climatology.

In the L31 model there is a clear overestimation of SSR in the stratocumulus areas and a strong underestimation of SSR over the tropical oceans. The L40 results are an improvement in both of these areas. More clouds and liquid water over the stratocumulus regions in the L40 version reduce the positive bias of the L31 model by decreasing the SSR by up to 50 W/m^2. In the ITCZ the L40 version produces less liquid water in the deep convection areas which contributes to a reduction of the SSR negative bias.

4.2.3 Net Surface Heat Flux

Figure 20(a) shows the global distribution of the Net Surface Flux (NSF) as given by the climatology of *Silva et al* (1994) for JJA. Figures 20(b) and 20(c) show respectively the NSF differences between the L31 model and the climatology and the L40 model and the climatology. Overall it can be seen that both models cool the ocean too much. This is already obvious from the analysis of the plots for SLHF and SSR which are the major components in the surface heat budget.

The L40 version reduces the positive bias that the L31 version experiences in the stratocumulus regions of the Pacific Ocean. Off the west coast of the United States and Mexico the bias is basically vanished while off the west

coast of South America the bias is gone in the stratocumulus region but still persists close to the equator. This positive bias is due to a positive bias in the SSR and SLHF, which is, in both cases, reduced by the L40 model.

The ocean cold bias pattern is fairly similar in both model versions. However, it can be said that there is a general improvement with the L40 version. In areas like the equatorial and the sub-tropical west Pacific (off the East coast of Australia) the L40 model produces substantial improvements. The NSF is also improved by the L40 model in the following areas: sub-tropics of North and South Pacific, tropics of the Atlantic and the Bay of Bengal. The L31 model is better in the sub-tropics of the South Atlantic.

4.3 General considerations

In general, the results show that the cloud cover, the longwave and shortwave top of the atmosphere fluxes, the precipitation and the surface fluxes are improved with the higher vertical resolution when compared with satellite data and surface climatology. However, the increased cloudiness in the L40 model introduces a small overall cooling in the model.

The higher resolution also leads to deeper boundary layers over the ocean. How realistic these deeper boundary layers are will be investigated in section 5, where comparisons against radiosondes are used in order to assess the quality of the inversion height simulations. The deeper L40 boundary layers are also responsible for a small cooling at around 850 hPa.

The L40 model's simulation of the Liquid Water Path (LWP) is also more realistic in the tropics and in the stratocumulus areas when compared with a climatology produced by *Weng et al.* (1997) (comparison not shown). This climatology uses the Special Sensor Microwave/Imager (SSM/I) to estimate the LWP. The increase of liquid water in the stratocumulus regions, as could be inferred from the discussion on section 3, provides a higher and more realistic LWP simulation with the L40 model. Over the tropical oceans the L40 model's LWP is reduced.

Similar overall results are achieved when the period December-January-February is analysed in detail. The sensitivity of the cloud and convection schemes to increased boundary layer vertical resolution, in particular in the sub-tropical regions, and the interaction between clouds and radiation is believed to be responsible for most of the impact of the L40 resolution in the climate simulations.

5. Data assimilation/forecast experiments

5.1 Forecast experiments and a low level jet

The impact of the improved boundary layer vertical resolution has also been investigated in the global ECMWF model in the context of 10 day forecasts at T213 resolution with CY15R6 and CY16R2. The forecasts are reasonably good and the impact on forecast performance measured in geopotential anomaly correlation is neutral. In general, the boundary layer structure has been improved with more realistic wind, temperature and moisture profiles. The temperature inversions are better resolved and the representation of stratocumulus has been improved as in the one-column simulations and the long integrations.

One of the physical processes that may benefit from enhanced vertical resolution are low-level jets, which are often linked with significant meteorological phenomena such as cyclogenesis and convection. A prominent low-

level jet (Fig. 21(a)) was observed along the U.S. East Coast on 24-26 January 1986 using special observing data taken during the Genesis of Atlantic Lows Experiment (GALE). Cold-air damming and intense lower-tropospheric sensible and latent heating near the Gulf Stream produced strong geostrophic forcing along the coast that resulted in a favourable mesoscale environment for low-level jet formation. The jet was observed to have a maximum at the 960 hPa level near the edge of the cold dome. Results from a mesoscale model *(Doyle and Warner*, 1993) indicate that two distinct wind speed maxima existed: one along a cold front over the Gulf Stream and a secondary more shallow jet along the North Carolina coast near the western edge of the Gulf Stream. For a more detailed discussion of the synoptic-scale and mesoscale forcing in this case see *Doyle and Warner* (1990).

Two 24 hour forecasts for the wind speed (at around 970 hPa) are shown in Figs. 21(b) and 21(c) for the L31 and L40 models, respectively. The L40 model version has a wind speed maximum in excess of 20 m s^1 over the Gulf Stream, which is about 10% stronger than the low-level jet in the L31 model and more in agreement with the mesoscale model results. More significantly, a coastal jet is present in the L40 model results (Fig. 21(c)) and is absent in the lower vertical resolution results (Fig. 21(b)). The existence of the coastal jet is in agreement with the observations (Fig. 21(a)) and once again the mesoscale model results. Thus, increased vertical resolution in the boundary layer is necessary for the simulation of the coastal low-level jet in this case.

In general, the overrall structure of the low level wind is much improved with the L40 model. The wind direction at the 10 m level during the night compares better with the SYNOP observations (up to improvements of about 5 degrees). This is to be expected since with the L40 model the 10 m wind is now a prognostic quantity and not a diagnostic one (as has been the case). In a study similar to the one presented in Beljaars et al. (1996) it was verified that the prediction of rain in the US Gulf coast, for summer 1993, is bettter with the L40 model. This is probably due to a more realistic low level wind and low level moisture transport in the L40 version.

5.2 3D-Var data assimilation performance

Assimilation experiments with the L40 vertical resolution were performed for two periods of two weeks each: one in summer (30 June 1996 - 14 July 1996) and the other in winter (1 February 1997 - 15 February 1997). The assimilation system uses the 3D-Var analysis scheme which is based on a variational approach. The experimental results and the operational implementation at ECMWF are described by *Andersson et al.* (1998). *Courtier et al.* (1998) analyse the formulation and the structure functions are described in *Rabier et al.* (1998). In order to perform data assimilation with the 40 level model new background error statistics have been computed based on 80 two-day forecasts, following the approach described in *Bouttier et al.* (1997).

In general the assimilations and the forecasts starting from the L40 analysis behave in a realistic way and the forecast performance is basically neutral. Global maps, at different pressure levels from the surface to 100 hPa, of the temperature and relative humidity differences between L31 and L40 5 day forecasts and their own analysis are similar for both model versions.

Statistics of observation departures from the first-guess and the analysis were analysed for both assimilation runs. The results show that in general there is not a major impact of the increased vertical resolution in the RMS and bias of the observation departures. The only serious impact is on the humidity fields. In fig. 22(a) and fig. 22(b)

the relative humidity bias in terms of SYNOP observations minus first guess (OBS-FG) and minus analysis (OBS-AN) is shown for the Tropics and the Southern Hemisphere. The data analysed corresponds to 14 days (00 UTC and 12 UTC) of the summer assimilation experiment. The values at 1000 hPa correspond to the layer of 1000-850 hPa, the ones at 850 hPa correspond to 850-700 hPa, the ones at 700 hPa to 700-500 hPa and the ones at 500 hPa to 500-400 hPa. It is clear from the figures that the L40 model fits the data much better. The OBS-FG is improved by up to 3% while the OBS-AN is improved by up to 1% of relative humidity.

In fig. 23(a) and 23(b) the same as in fig. 22 is shown, but for the TEMP observations. In this case also included are values at 400 hPA which corresponds to the layer 400-300 hPa, 300 hPa that corresponds to 300-250 hPa, 250 hPa that corresponds to the layer 250-200 hPa and 200 hPa that corresponds to 200-150 hPa. The improvement in the boundary layer relative humidity bias due to the increased resolution is also clear in these figures. However, in the tropical free troposphere the results are a bit worse than with the L31 model. A similar type of results are also obtained during the winter experiment and because of this will not be shown here. In the corresponding RMS plots the impact of the L40 version is not so clear.

The amount of observations used by both models (L31 and L40) is very much the same. Again the only exception is on the use of humidity observations. The L40 version uses more relative humidity observations than the L31 model. In particular the number of SYNOP observations used in the Tropics and the Southern Hemisphere can increase, with the L40 model, by up to almost 1% (in a total of about 10000 observations used in 14 days at 00 UTC and 12 UTC).

5.3 The boundary layer height - comparison against radiosondes

The L40 resolution leads to deeper boundary layers over the ocean. In order to investigate how realistic these deeper boundary layers are, a detailed comparison between radiosondes and the L31 and L40 model derived profiles has been carried out. L31 and L40 forecasts starting from their own analysis are compared against radiosondes from 10 locations over the ocean (see table 1 where the radiosondes locations are shown). These correspond to island stations located in the Atlantic and Indian oceans. The height of each station is usually not much above sea level.

In the first set of comparisons, L31 and L40 24 h forecasts starting from their own analysis were compared against radiosondes for these 10 locations. 12 days were analysed which gives a total of 120 radiosondes, from which 86 were selected. The ones that were not selected correspond to situations where the inversion was not clearly defined. These days correspond to forecasts verifying on 2 June 1996 to 13 June 1996.

The results for the inversion height, the root-mean-square (RMS) error and the bias, when compared with the observations, of the L31 and L40 forecasts are shown in table 2. It can be seen that the observed mean inversion height for these 10 locations is about 855 hPa, whereas in the L31 forecasts is about 867 hPa and in the L40 model is about 857 hPa. This gives a bias of almost 12 hPa for the L31 model and almost 2 hPa for the L40 model. The RMS error, on the other hand is significant for both cases, but again the results are better for the L40 version (an RMS error of almost 31 hPa) than for the L31 model (an RMS error of about 41 hPa).

STATION	Latitude	Longitude
SAL (cape Verde)	16.73	-22.95
MARTIN DE VIVIES (Ile Amsterdam)	-37.8	77.53
FORT-DAUPHIN (Madagascar)	-25.03	46.95
VACOAS (Mauritius)	-20.3	57.5
FUNCHAL (Madeira)	32.63	-16.9
SEYCHELLES INTER. A/P	-4.68	55.53
TENERIFE (Canary Is.)	28.45	-16.25
ST. HELENA IS.	-15.93	-5.67
WIDE AWAKE FIELD (Ascension Is.)	-7.97	-14.4
DIEGO GARCIA	-7.35	72.48

Table 1: The 10 radiosondes locations (see text for details).

In fig. 24 a scatter plot of the observed versus the model (L31 and L40 24 h forecasts) inversion height is shown. It can be seen that in the L31 model, above 950 hPa, the boundary layer is consistently shallower than in the observations. The L40 model results do not have such a pronounced bias. However, the L40 model slightly overestimates the boundary layer depth from the surface until around 900 hPa and slightly underestimates it above 850 hPa. This analysis confirms the results from table 2.

	PBL height (hPa)	Bias (hPa)	RMS error (hPa)
Observations	855	-	-
L31 Model	867	12	41
L40 Model	857	2	31

Table 2: Inversion height, the root-mean-square (RMS) error and the bias of the model inversion height, when compared with the observations, of the L31 and L40 24 h forecasts. Units in hPa.

From these results it seems that, for the 24h forecasts, the L40 boundary layer is 10 hPa deeper than in the L31 model and is closer to the observations: both the bias and the RMS error are 10 hPa smaller in the L40 model than in the L31 version.

In the second set of comparisons, L31 and L40 120 h forecasts starting from their own analysis were compared against radiosondes from the same 10 locations. Again 12 days were analysed which gives a total of 120 radiosondes, from which 103 were selected. These days correspond to forecasts verifying on 6 June 1996 to 17 June 1996.

The results for the inversion height, the RMS error and the bias of the L31 and L40 forecasts are shown in table 3. The observed mean inversion height for these 10 locations is about 833 hPa. This value is slightly different from the mean height of the first set because the verifying dates are shifted by 4 days and also because of a certain degree of subjectivity of the method used to estimate the inversion height. In the L31 120 h forecasts the inversion hight is about 857 hPa and in the L40 model is about 843 hPa. This gives a bias of about 24 hPa for the L31 model and about 10 hPa for the L40 model. The RMS error, on the other hand is significant for both cases, but again the results are better for the L40 version (an RMS error of almost 36 hPa) than for the L31 model (an RMS error of about 51 hPa). The differences in bias and RMS error between the first and the second set of comparisons reflects the error growth from 24 to 120 hours.

	PBL height (hPa)	Bias (hPa)	RMS error (hPa)
Observations	833	-	-
L31 Model	857	24	51
L40 Model	843	10	36

Table 3: As in table 2 but fot the 120 h forecasts

In fig. 25 a scatter plot of the observed versus the model (L31 and L40 120 h forecasts) inversion height is shown. It can be seen that the results for both models are clearly worse when compared to fig. 24 and that again in the L31 model the boundary layer is consistently shallower than in the observations. The L40 model results are better with the shallow boundary layer depth bias not so pronounced as in the L31 model. These results confirm the analysis from table 3.

Both models overestimate the boundary layer depth up to a certain height and underestimate it above that height. This happens in the 24 h and in the 120 h forecasts and it is interesting to note that the height where the models start to underestimate the inversion depth (which is different for both models) is similar in the 24 h and 120 h forecast for each resolution version.

For the 120 h forecasts the L40 boundary layer is 15 hPa deeper than in the L31 model and is again closer to the observations: both the bias and the RMS error are about 15 hPa smaller in the L40 model than in the L31 version.

5.4 4D-Var data assimilation/forecast experiments

Experimentation has also been carried out using CY18R6 of the ECWMF analysis/forecast system. Compared to the 3D-Var version (CY16R2), used in sections 5.2 and 5.3, the new system contains several changes: The Four-Dimensional Variational assimilation (4D-Var) was implemented operationally in November 1997 (*Rabier et al.*, 1997); revised parametrizations were introduced operationally in December 1997 (*Gregory et al.*, 1998); the TL319 linear grid, the new orography and changes to the two-time level scheme were introduced in April 1998 (*Hortal*, 1998(a), 1998(b)); The coupled atmosphere-wave model (*Janssen et al.*, 1998) and the use of temperatures and significant level data from radiosondes (*Unden and Andersson*, 1998) will be introduced operationally in June 1998.

All of these changes are supposed to have some influence on the performance of the L40 system but the new orography and in particular the use of temperatures and significant level data are expected to have a noticeable impact on the results to be obtained with the new L40 version of the ECMWf analysis/forecast system.

4D-Var assimilation experiments, with the L40 vertical resolution, were performed for two periods of 17 days each: a spring experiment (15 May 1997 to 31 May 1997) and a winter experiment (28 November 1997 to 15 December 1997). An analysis of the statistics of observation departures from the first-guess and the analysis was performed. As in the 3D-Var assimilations the results show that there is not a significant impact of the L40 model in the RMS and bias of the observation departures.

Again the major impact is on the humidity fields. The L40 model fits the relative humidity SYNOP and TEMP observations better than the L31 model. The results are similar to the ones presented for the 3D-Var experiments but the impact of the L40 model in the 4D-Var humidity is also noticeable in the Northern Hemisphere in the spring.

In fig. 26(a) the relative humidity bias in terms of SYNOP observations minus first guess (OBS-FG) and minus analysis (OBS-AN) is shown for the Tropics. The data corresponds to 14 days (00 UTC and 12 UTC) of the spring assimilation experiment. Fig. 26(a) shows again that the L40 model fits the data much better. The OBS-FG can be improved by up to 4% relative humidity, with the L40 OBS-FG bias being smaller than the L31 OBS-AN bias.

In fig. 26(b) the same as in fig. 26(a) is shown, but for the TEMP observations. The improvement in the boundary layer relative humidity bias due to the increased resolution is again clear. The 4D-Var results are even better than the 3D-Var ones, since in the tropical free troposphere the L40 relative humidity bias is smaller than with the L31 model. Similar results are obtained for the winter experiment and will not be shown here.

In the 4D-Var experiments, a positive impact from the L40 version can also be seen on the statistics of the temperature radiosonde observation departures in the Tropics. This can be seeen in fig. 27(a) and fig. 27(b) where the temperature bias in terms of tropical TEMP observations minus first guess (OBS-FG) and minus analysis (OBS-AN) for the spring and winter experiments (14 days of each experiment) is shown. The L40 OBS-AN bias is always smaller than the corresponding L31 bias and the L40 OBS-FG results are particularly good in the tropical free troposphere, between 700 hPa and 200 hPa. The improvements in the temperature bias can go up to almost 0.3 K at some levels. The amount of observations used by both models is similar and, as in 3D-Var, the only significant exception is that more humidity observations are used by the L40 version.

The L40 and L31 model forecasts are evaluated in terms of anomaly correlation scores. The 17 spring forecasts scores for the 500 hPa geopotential for the Northern Hemisphere, Southern Hemisphere and Europe are shown in fig. 28. For the Northern Hemisphere the results are basically neutral with a very small advantage for the L40 model from day 5 to day 7.5. For the Southern Hemisphere the results are neutral with a slight advantage for the L31 model between days 2 and 4 and for the L40 model between days 4 and 6. The performance of the L40 forecasts over Europe is clearly better than with the L31 model and this is already quite clear after day 3. A

similar picture is present in the 1000 hPa scores, but even more neutral. However, the better L40 model performance over Europe is quite clear at 1000 hPa as well. When the anomaly correlation scores are substantially below the 60% line, the different model performances during the last part of the 10 day forecasts is usually not taken into account.

The scatter plots of the 120 hour forecasts for the 500 hPa geopotential anomaly correlation are shown in fig. 29. It can be seen that the scatter between the forecasts is smalll and that the L40 forecasts are in general better for the Northern and the Southern Hemispheres, but are particularly good over Europe.

The 18 winter forecasts scores for the 500 hPa geopotential for the Northern Hemisphere, Southern Hemisphere and Europe are shown in fig. 30. In the Northern Hemisphere the results are positive for the L40 model from day 5 and in the Southern Hemisphere the results are much more neutral. The L40 forecasts over Europe are again better than the L31 model and this is clear after day 4. In the 1000 hPa scores (not shown) the results are more neutral but the better L40 model performance over Europe is still quite clear. The scatter plots of the Winter forecasts are not shown because the results are very neutral.

The 35 (winter and spring) forecasts mean error (bias) scores for the 500 hPa geopotential, Northern and Southern Hemisphere, are shown in fig 31. It is quite clear that the L40 model performance is much better than the L31 model. The positive bias grows during the simulations in both model versions, however the L40 model bias is always smaller and the difference between the two model biases becomes larger with time.

In terms of temperature scores the anomaly correlation for 17 spring 850 hPa temperature forecasts, for the Northern and Southern Hemisphere and the Tropics, is shown in fig. 32. It can be seen that the L40 model is better than the L31 at 850 hPa in the Tropics and in the Southern Hemisphere and is basically neutral in the Northern Hemisphere. The 18 Winter forecasts (not shown) provide similar results with the exception that the results for the Southern Hemisphere are more neutral.

The mean 850 hPa temperature error (bias) of the 35 (winter and spring) forecasts, for the Northern and Southern Hemisphere and the Tropics, is shown in fig. 33. It is clear from these figures that the L40 temperature bias is always substantially smaller than the L31 bias. The performance of the L40 model in the Northern Hemisphere is particularly impressive in this respect: the L40 bias is almost negligible during the 10 forecast days while the L31 bias grows up to almost 0.4 K.

The anomaly correlation scores for the 200 hPa temperature for the 17 spring forecasts is shown in fig. 34. At 200 hPa the L40 temperature performance is neutral in the Northern and Southern Hemisphere but is worse than the L31 model in the Tropics. These temperature results can be confirmed by the analysis of global maps of 5 day forecasts minus analysis (not shown). In there it can be seen that, globally, the boundary layer temperature structure of the L40 forecasts is more realistic, when compared with the analysis, than the L31 model. On the contrary, at 200 hPa the differences between the forecasts and the analysis show that the L40 model temperature in the Tropics is less realistic (warmer than the L31 model by about 0.5 K).

The performance of the L40 model forecasts is basically neutral in terms of 850 hPa and 200 hPa vector wind anomaly correlation (not shown), in the Southern and Northern Hemisphere and in the Tropics.

From the analysis of the atmospheric and hydrological budget of the 17 spring L40 and L31 forecasts it can be seen that the L40 model reduces the spin-down of convection over the Tropics by as much as 20 W/m^2 in the first 12 hours. The same is true for the condensation but in a much smaller scale. An improvement in the spin-down by the L40 model can also be seen in the precipitation over the Tropics where the initial precipitation spin-down is improved by more than 0.5 mm/day in the first 12 hours, as can be seen in fig. 35(a), corresponding to the L31 forecasts, and fig. 35(b) corresponding to the L40 model. Over the ocean this improvemnet goes up to about 1 mm/day. Similar results are achieved in the winter forecasts.

This improvement in the spin-down is consistent with the reduction of the L40 analysis/first-guess humidity bias when compared against TEMP and SYNOP observations. An improvement, with the L40 model, in the low level tropical humidity structure is also apparent when forecasted values of specific and relative humidity are compared against climatology and local observations.

6. Conclusions

A new configuration of enhanced vertical resolution (L40) was presented. The main differences between the new version and the operational L31 model are: i) the height of the lowest model level of the L40 configuration is at about 10 m above the model surface, while the L31 lowest model level height is about 33 m; ii) the lower troposphere resolution is significantly increased with the new version and in the first 1500 m above the surface the L40 model has twice the number of levels (12) than the L31 version (6); iii) in the new version the worst resolution (in pressure) is now at about 575 hPa while in the L31 model is around 730 hPa.

The first tests were performed using the one-column model to simulate the ASTEX Lagrangian 1 experiment. With the L31 model there is a reasonable simulation of the transition from a low level stratified cloud to a shallow cumulus situation. However, during the transition the model looses nearly all liquid water, which is unrealistic. The stratocumulus clouds and the transition to cumulus clouds is better captured with the increased resolution: the liquid water does not disappear in the L40 version and the liquid water values in the stratocumulus are more realistic. However, the L40 model boundary layer becomes too deep and the liquid water too high in the shallow cumuli region.

A detailed analysis of the evolution of the source and sink terms of the liquid water equation shows that the absolute values of all the tendencies are larger in the L40 version. Some of these terms are larger because shallow convection is more frequent and intense in the L40 version. The liquid water does not disappear in the L40 version as in the L31 version because the detrainment from convection is in general higher than the evaporation during the transition period. The L40 LWP evolution in the stratocumulus regime is more realistic when compared to the observations. In the shallow convection regime both model versions have LWP values that are clearly too high. The vertical structure of the cloud fraction in the L40 model is much closer to the observations.

In the long integrations (120 days), the cloud cover in the L40 configuration has in general increased when compared with the L31 model, which is clearly an improvement compared to ISCCP observations. This is particularly true over the stratocumulus areas and the southern ocean where there are improvements of up to 50% with the higher vertical resolution. In the stratocumulus areas the increase of clouds with the L40 resolution creates a better agreement with the Top Shortwave Radiation observations from ERBE. In fact the positive bias of the L31 model in these regions is reduced by the new resolution by as much as 15 to 30 W/m2.

The high vertical resolution reduces the positive OLR bias over the tropical oceans (when compared with ERBE). The L40 model also makes a much better simulation of precipitation in the equatorial regions. In the ITCZ over the Pacific the L40 model reduces significantly the positive bias from the L31 model. In some areas the error is reduced by more than 8 mm/day (in a total error of up to 16 mm/day in the L31 model). The L40 and L31 long integration results were also compared with a climatology of surface fluxes. In many areas, particularly in the stratocumulus region, there are significant improvements with the L40 version in the latent heat flux, the surface shortwave radiation and consequently in the net surface flux. The L40 model LWP is also more realistic in the tropics and in the stratocumulus areas when compared with a climatology.

Results from T213 forecasts have shown that the representation of boundary layer inversions and the low level wind structure is more realistic with the L40 model. A coastal low level jet, observed during GALE, is simulated in a very realistic way by the L40 version of the forecast model. The L31 version is not able to produce such a jet.

L40 and L31 3D-Var assimilation experiments were performed for two periods of two weeks. The results show that the forecast performance is basically neutral and that there are no major differences in the 5 day forecast systematic errors. It is clear that the L40 model fits the SYNOP and TEMP relative humidity observations better than the L31 model and uses more humidity observations than the L31 model.

The performance of the assimilation and forecasting system in predicting the boundary layer inversion height has been analysed. A detailed comparison between radiosondes and L31 and L40 forecasts (24 h and 120 h) starting from their own analysis has been carried out. In the L31 model the boundary layer is consistently shallower than in the observations. In the 24 h forecasts, the L40 boundary layer is 10 hPa deeper than in the L31 model and in the 120 h forecasts the L40 boundary layer is 15 hPa deeper than in the L31 model. In both cases the L40 inversion height is closer to the observations.

4D-Var assimilation experimentation with the most recent model cycle (CY18R6) was carried out for two periods (winter and spring). An analysis of the statistics of observation departures from the first-guess and the analysis shows that, as in 3D-Var, the L40 model fits the tropical relative humidity SYNOP and TEMP observations better than the L31 model. A positive impact from the L40 version is also clear on the statistics of the tropical temperature TEMP observation departures.

The 17 spring forecasts scores (anomaly correlation) for the 500 hPa geopotential are basically neutral for the Northern and Southern Hemispheres, but for Europe the performance of the L40 forecasts is clearly better. Scatter plots of the 5 day forecasts show that the L40 forecasts are slightly better for the Northern and Southern

Hemispheres and particularly good over Europe. The 18 winter forecasts scores for the 500 hPa geopotential are positive for the Northern Hemisphere and Europe and are more neutral for the Southern Hemisphere. The 500 hPa geopotential mean error for the winter and spring forecats, in the Northern and Southern Hemisphere, is much smaller with the L40 model.

The 850 hPa temperature scores, in terms of anomaly correlation, show that the L40 model is better than the L31 in the Tropics and is neutral in the Southern and Northern Hemispheres. However, the mean 850 hPa temperature error (bias) of the 35 (winter and spring) forecasts, for the Northern and Southern Hemisphere and the Tropics, is much smaller with the L40 model. At 200 hPa the L40 performance is basically neutral in the Northern and Southern Hemisphere but is worse in the Tropics.

The analysis of the atmospheric and hydrological budgets shows that the L40 version reduces the spin-down of convection and precipitation over the Tropics. The initial precipitation spin-down is improved by more than 0.5 mm/day in the first 12 hours. These results in the spin-down are quite significant and are consistent with an overall improvement of the tropical humidity structure in the L40 version of the model. Significantly this overrall improvement also includes a reduction of the L40 analysis/first-guess humidity bias, when compared against TEMP and SYNOP observations, and a reduction of the tropical precipitation bias in long integrations.

Acknowledgements

References

Anderson, D., T. Stockdale, J. Alves, M. Balmaseda and J. Segschneider, 1997: Seasonal Forecasting at ECMWF. *ECMWF Newsletter Number 77*, Autumn 1997, ECMWF, Reading, United Kingdom, 2-8.

Andersson, E., J. Haseler, P. Undén, P. Courtier, G. Kelly, D. Vasiljevic, C. Brankovic, C. Cardinali, C.Gaffard, A. Hollingsworth, C. Jakob, P. Janssen, E. Klinker,A. Lanzinger, M. Miller, F. Rabier, A. Simmons, B. Strauss, J-N. Thepaut and P. Viterbo, 1998: The ECMWF implementation of three dimensional variational assimilation (3D-Var). Part III: Experimental Results. *Q. J. R. Meteorol. Soc.* Vol.124, 1831-1860.

Barkstrom, B.R., and G.L. Smith, 1986: The Earth Radiation Budget Experiment: Science and implementation. *J. Geophys. Res.*, 24, 379-390.

Beljaars, A.C.M., 1991: Numerical schemes for parametrizations. Seminar proc. on Numerical Methods in Atmospheric Models. ECMWF. september 1991. Vol.2, pp. 1-42.

Beljaars, A.C.M., P. Viterbo, M. Miller, and A.K. Betts, 1996: The anomalous rainfall over the USA during July 1993: Sensitivity to land surface parametrization and soil moisture anomalies. *Mon. Wea. Rev.*, 124, 362-383.

Boville, B.A. and W.J. Randel, 1992: Equatorial Waves in a Stratospheric GCM: Effects of Vertical Resolution. *J.Atmos.Sci.*, 49, 785-801.

Bouttier, F., J. Derber and M. Fisher, 1997: The 1997 revision of the Jb term in 3D/4D-var. *ECMWF Technical Memorandum No. 238*. ECMWF, Reading, United Kingdom.54 pp.

Bretherton, C.S., and R. Pincus, 1995: Cloudiness and marine boundary layer dynamics in the ASTEX Lagrangian experiments. *J.Atmos.Sci.*, **52**, 2707-2723.

Courtier, P., E. Andersson, W. Heckley, J. Pailleux, D. Vasiljevic, M. Hamrud, A. Hollingsworth, F.Rabier and M. Fisher, 1998: The ECMWF implementation of three dimensional variational assimilation (3D-Var). Part I: Formulation. *Q. J. R. Meteorol. Soc.* Vol.124, 1783-1808.

de Roode, S.R., and P.G. Duynkerke, 1997: Observed Lagrangian Transition of Stratocumulus into Cumulus During ASTEX: Mean State and Turbulence Structure. *J. Atmos. Sci.*, 54, 2157-2173.

Delage, Y., 1988: The position of the lowest levels in the boundary layer of atmospheric circulation models, *Atmos. Ocean*, 26, 329-340.

Doyle, J.D., and T.T. Warner, 1990: Mesoscale coastal processes during GALE IOP 2. *Mon. Wea. Rev.*, **118**, 283-308.

Doyle, J.D., and T.T. Warner, 1993: A three-dimensional numerical investigation of a Carolina coastal low-level jet during GALE IOP2. *Mon. Wea. Rev.*, **121**, 1030-1047.

Duynkerke, P.G. and A.G.M. Driedonks, 1987: A model for the turbulent structure of the stratocumulus-topped atmospheric boundary layer. *J. Atmos. Sci.*, 44, 43-64.

Girard, C. and Y. Delage, 1990: Stable schemes for the vertical diffusion in atmospheric circulation models, *Mon. Weather Rev.*, 118, 737-746.

Gregory, D., A. Bushell and A. Brown, 1998a: The interaction of Convective and Turbulent Fluxes in General Circulation Models. In Global Energy and Water Cycles. Report of the GEWEX conference of July 1994. Ed. Gurney and Browning. To be published by Cambridge University Press.

Gregory, D., J.J. Morcrette, C. Jakob and A. Beljaars, 1998b: Introduction of revised parametrizations of physical processes into the IFS. *ECMWF Newsletter Number 79*, Spring 1998, ECMWF, Reading, United Kingdom, 2-7.

Hortal, M., 1998 (a): New two-time-level semi-Lagrangian scheme. RD Memorandum R60.5/MH/12, February 1998, 18 pp.

Hortal, M., 1998 (b): TL319 resolution and revised orographies. RD Memorandum, R60.5/MH/23, March 1998, 18 pp.

Huffman, G.J., R.F. Adler, P. Arkin, A. Chang, R. Ferraro, A. Gruber, J. Janowiak, A. McNab, B. Rudolf, and U. Schneider, 1997: The Global Precipitation Climatology Project (GPCP) combined precipitation dataset. *BAMS*, 78, 5-20.

Jakob, C., 1998: Clouds in the ECMWF Re-Analysis. To be published in *J. Climate*.

Janssen, P A E M, Doyle J D, Bidlot J, Hansen B, Isaksen L and P Viterbo, 1998: Impact of Ocean Waves on the Atmosphere. Seminar on *Atmosphere-Surface interaction*, 8-12 September at ECMWF, Shinfield Park, Reading, UK.

Kitoh, A. and T. Tokioka, 1986: On the effects of vertical resolution on medium-range weather forecasts. In *Short- and medium-range weather prediction*. Ed. T. Matsuno. Meteorological Society of Japan. pp. 273-280.

Lenderink, G. and A.A.M. Holtslag, 1998: Evaluation of the kinetic energy approach for modelling turbulent fluxes in stratocumulus. Submitted to *Mon. Wea. Rev.*

Lindzen, R.S. and M. Fox-Rabinovitz, 1989: Consistent vertical and horizontal resolution, *Mon. Weather Rev.*, 117, 2975-2583.

Rabier, F., A. McNally, E. Andersson, P. Courtier, P. Unden, J. Eyre, A. Hollingsworth and F. Bouttier, 1997: The ECMWF implementation of three dimensional variational assimilation (3D-Var). Part II: Structure functions. *Q. J. R. Meteorol. Soc.* Vol.124, 1809-1830.

Rabier, F. and co-authors, 1998: Recent experimentation on 4D-Var and first results from a simplified Kalman filter. *ECMWF Technical memorandum No.240*, November 1997, ECMWF, Reading, UK, 42 pp.

Räisänen, P., 1996: The effect of vertical resolution on clear-sky radiation calculations. *Tellus*, 48A, 403-423.

Rossow, W.B., and R.A. Schiffer, 1991: ISCCP cloud data products. *BAMS*, 72, 2-20.

Simmons, A.J., 1979: Forecasting experiments using an alternative distribution of levels. *ECMWF Tech. Memo No.3.* pp.20.

Simmons, A.J., 1991: Development of a high resolution, semi-Lagrangian version of the ECMWF forecast model. Seminar proc. on Numerical Methods in Atmospheric Models. ECMWF, September 1991. Vol. II, pp. 281-324.

Simmons, A.J., 1994: Some stratospheric aspects of model development at ECMWF. Workshop proc. on *Stratosphere and Numerical Weather Prediction*, ECMWF, November 1993. pp. 23-59.

Silva, A.M., C.C. Young and S. Levitus, 1994: Atlas of surface marine data 1994 volume 1: algorithms and procedures. NOOA, Washington, USA. pp. 83.

Stockdale, T.N., D.L.T. Anderson, J.O.S. Alves and M.A. Balmaseda, 1998: Global seasonal rainfall forecasts using a couple ocean-atmosphere model. *Nature*, vol.392, p. 370-373.

Stull, R.B., 1989: *An Itroduction to Boundary Layer Meteorology*. Kluwer Academic Publishers. pp. 666.

Teixeira, J., 1997: Simulation of fog with the ECMWF prognostic cloud scheme. *ECMWF Technical Memorandum No. 225*. ECMWF, Reading, United Kingdom. November 1997, pp. 35.

Teixeira, J., C. Jakob and M. Miller, 1996: Simulation of ASTEX Lagrangian I with the ECMWF One-Column Model. in *Research Activities in Atmospheric and Oceanic Modelling*. Ed. A. Staniforth, February 1996. 4.45-4.46.

Tiedtke, M., 1993: Representation of Clouds in Large-Scale Models. *Mon. Weather Rev.*, 121, 3040-3061.

Unden, P., and E. Andersson, 1998: Use of temperatures and significant level data from radisondes. RD Memorandum R43/PU/20/DA, February 1998, 13 pp.

Untch, A., J.J. Morcrette and M. Hortal, 1996: ECMWF model with increased resolution in the stratosphere. in *Research Activities in Atmospheric and Oceanic Modelling*. Ed. A. Staniforth, February 1996. 3.40- 3.41.

Van Meijgaard, E. and A.P. van Ulden, 1998: A first order mixing-condensation scheme for nocturnal stratocumulus. To be published in *Atmos. res.*.

Welch, R.M, M.G. Ravichandran, and S.K. Cox, 1985: Prediction of quasi-periodic oscillations in radiation fogs. Part I: comparison of simple similarity approaches. *J. Atmos. Sci.*, 43, 633-651.

Weng F., N.C. Grody, R. Ferraro, A. Basist and D. Forsyth, 1997: Cloud Liquid Water Climatology from the Special Sensor Microwave/Imager. *J. Climate*. 10, 1086-1098.

Williamson, D.L. and J.G. Olson, 1998: A Comparison of Semi-Lagrangian and Eulerian Polar Climate Simulations. *Mon. Wea. Rev.*, 126, 991-1000.

Williamson, D.L., J.G. Olson and B.B. Boville, 1998: A Comparison of Semi-Lagrangian and Eulerian Tropical Climate Simulations. *Mon. Wea. Rev.*, 126, 1001-1012.
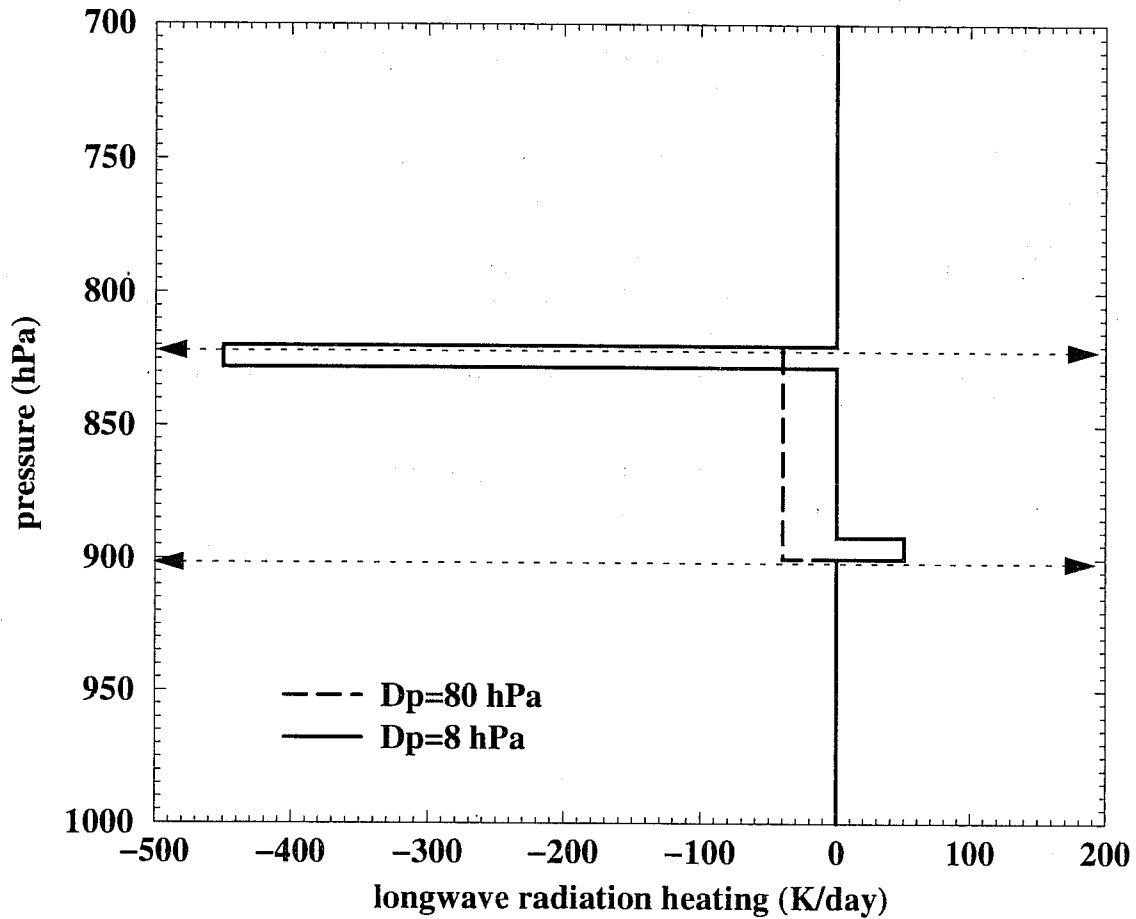
Fig. 1   Longwave radiative cooling for a cloud between 820 hPa and 900 hPa, with two different vertical resolutions: 80 hPa and 8 hPa.
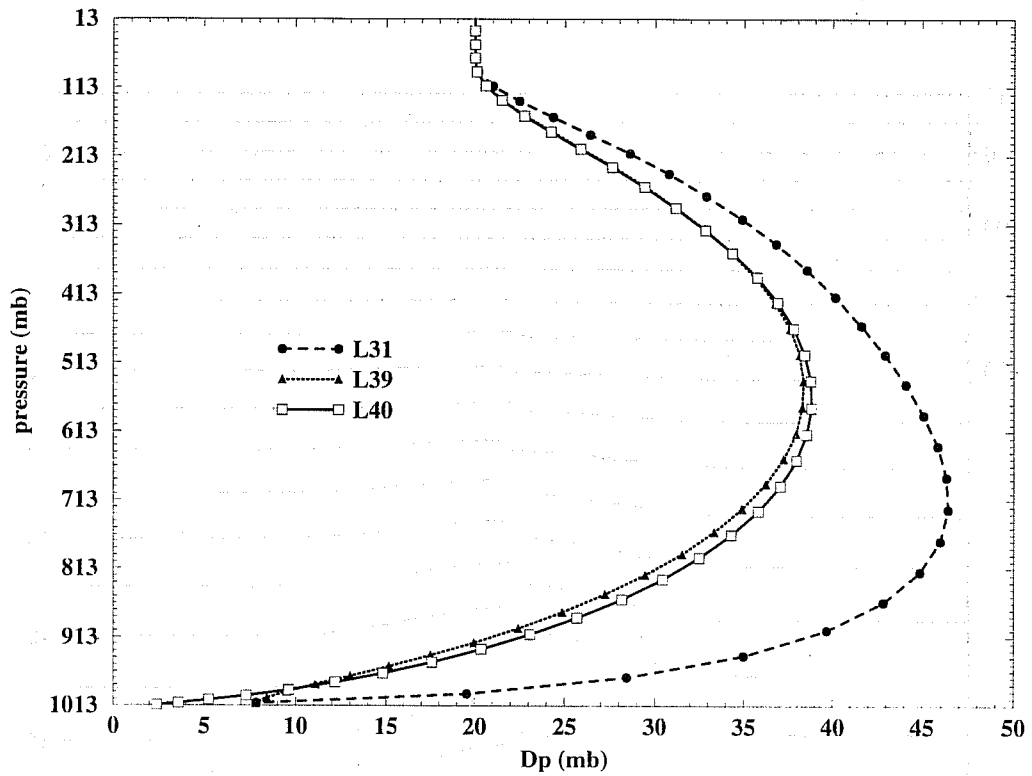
Fig. 2 The model-layer pressure thickness and the corresponding pressure of the model level for the enhanced L40 and L39 vertical resolution configurations and the L31 operational model.
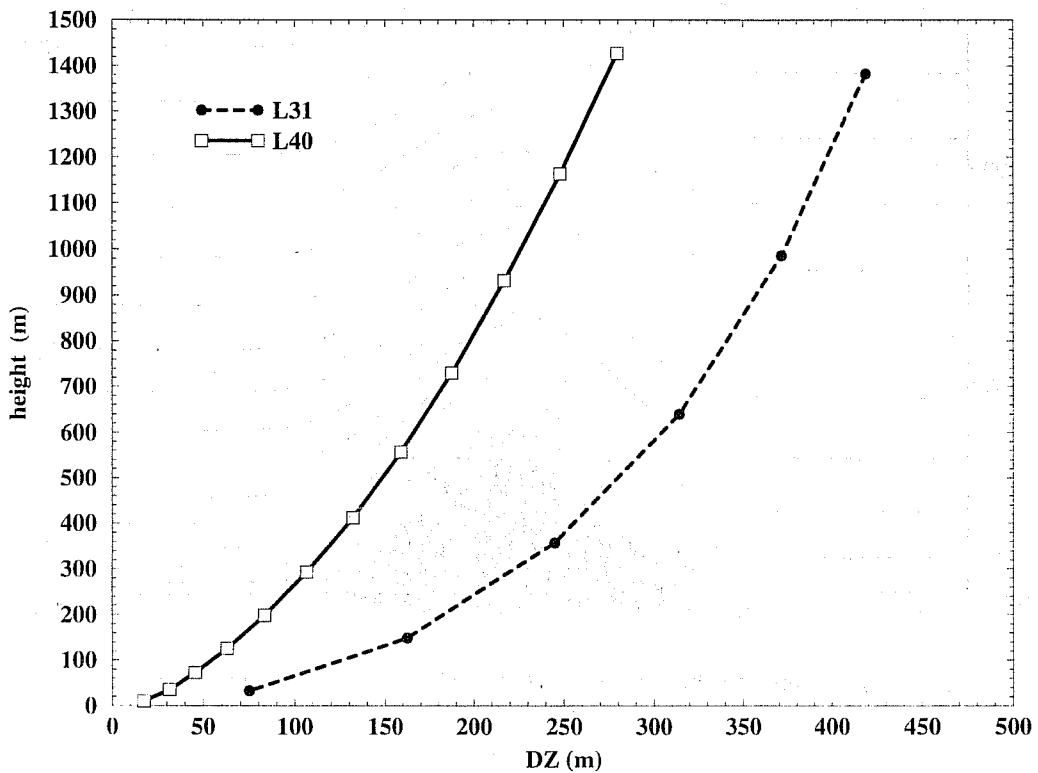
Fig. 3 The distribution in height of the L40 and L31 model-layer height thicknesses, for the first 1500 m above the surface.
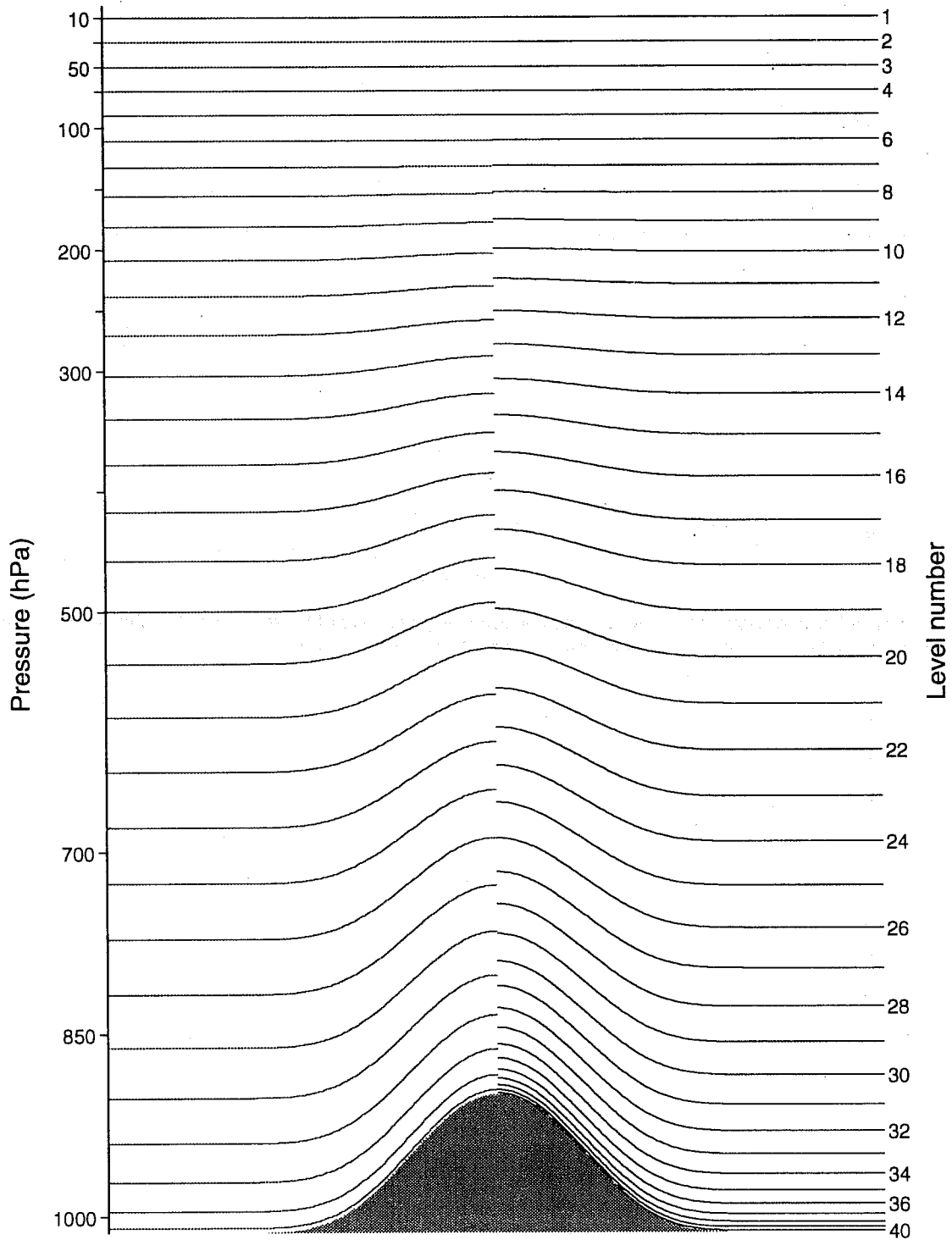
Fig. 4   The distribution of full model levels for the L31 and L40 configurations.
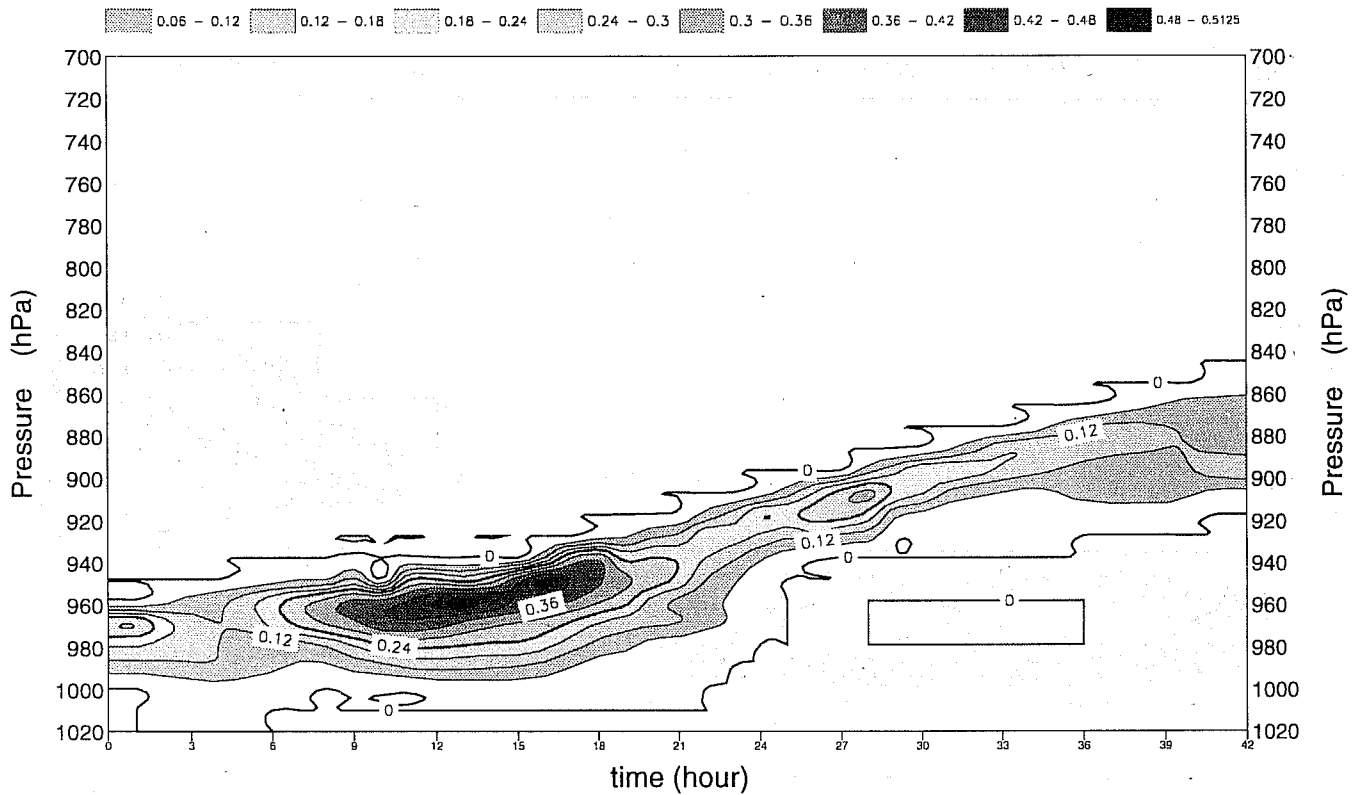
Fig. 5   The hourly observations of the liquid water profile (in g/kg). These observations are in a 10 hPa vertical grid resolution.
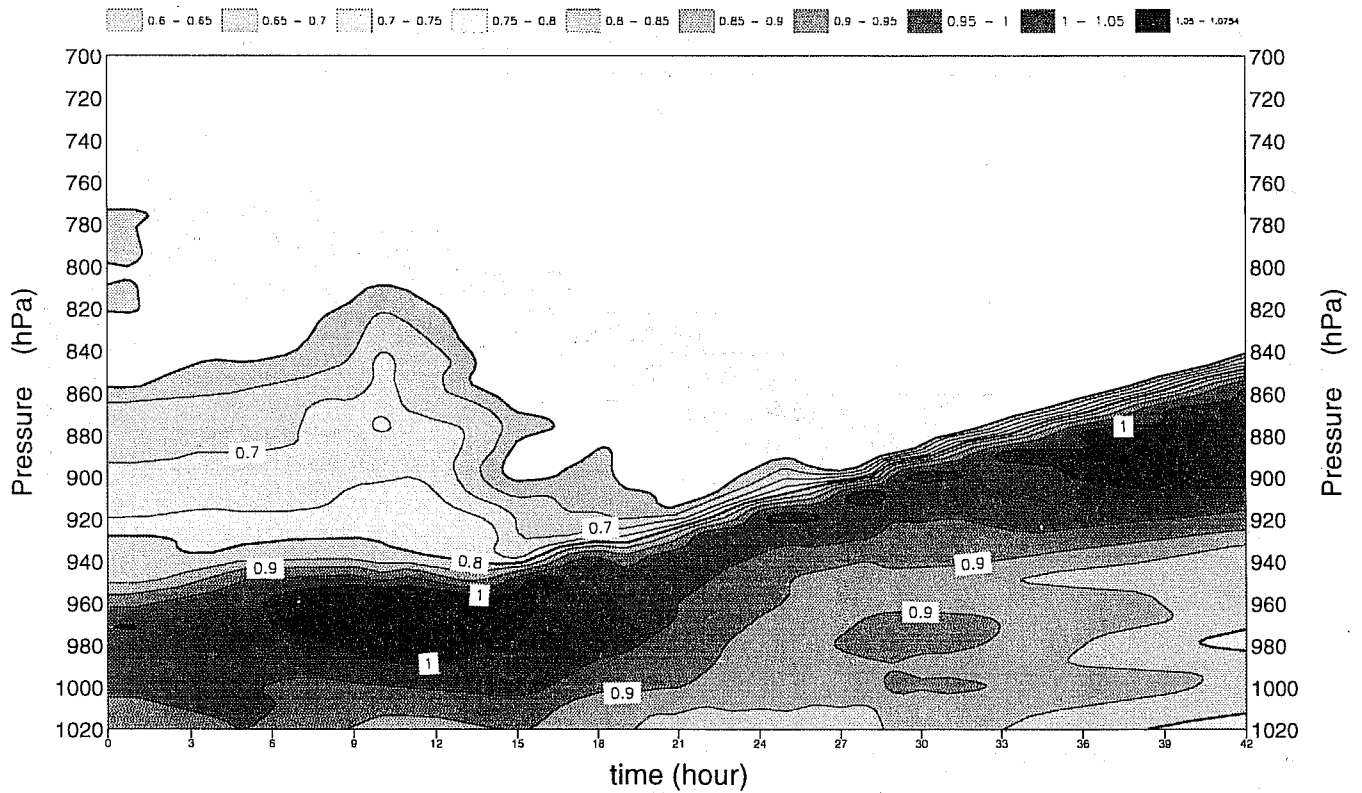
Fig. 6   The same as in fig.5 but for the relative humidity.
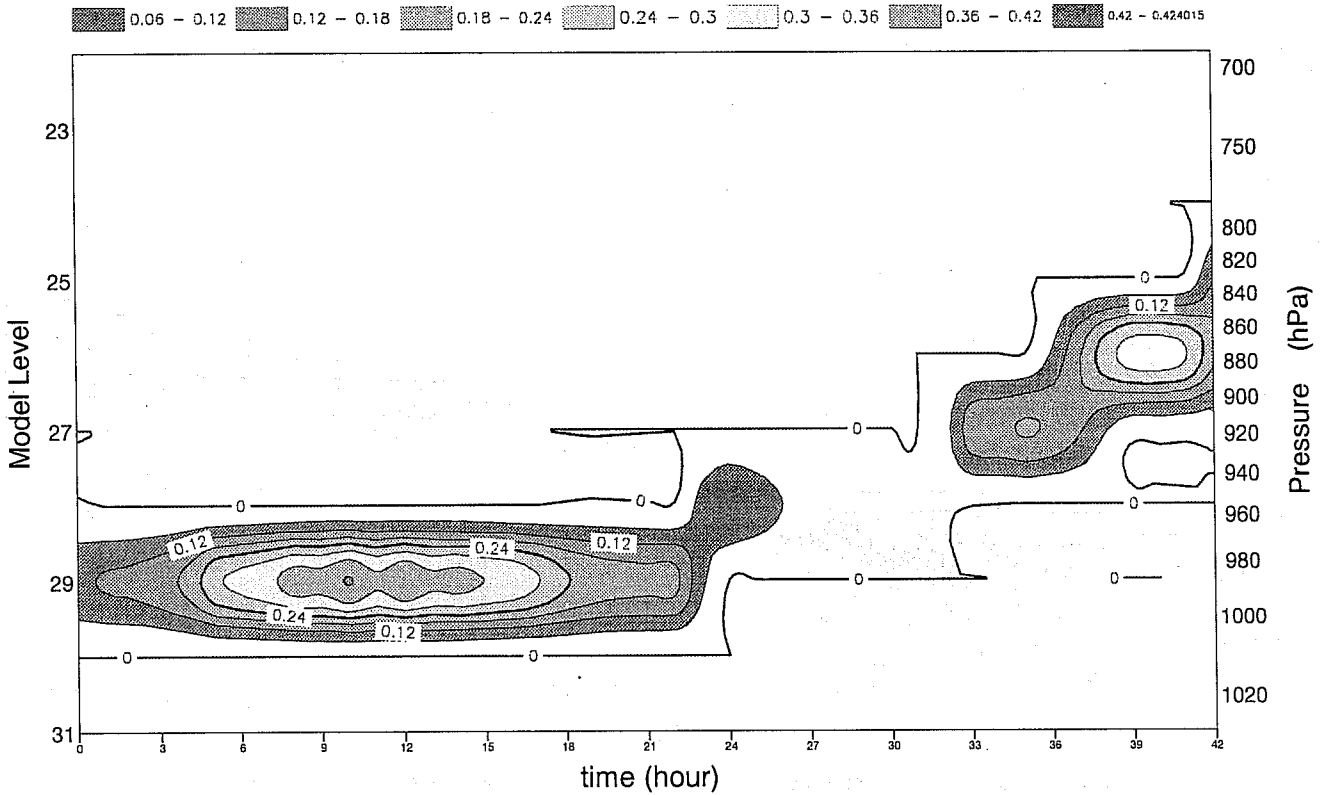
Fig. 7   The simulated hourly mean liquid water (g/kg) at different levels produced by the L31 model.
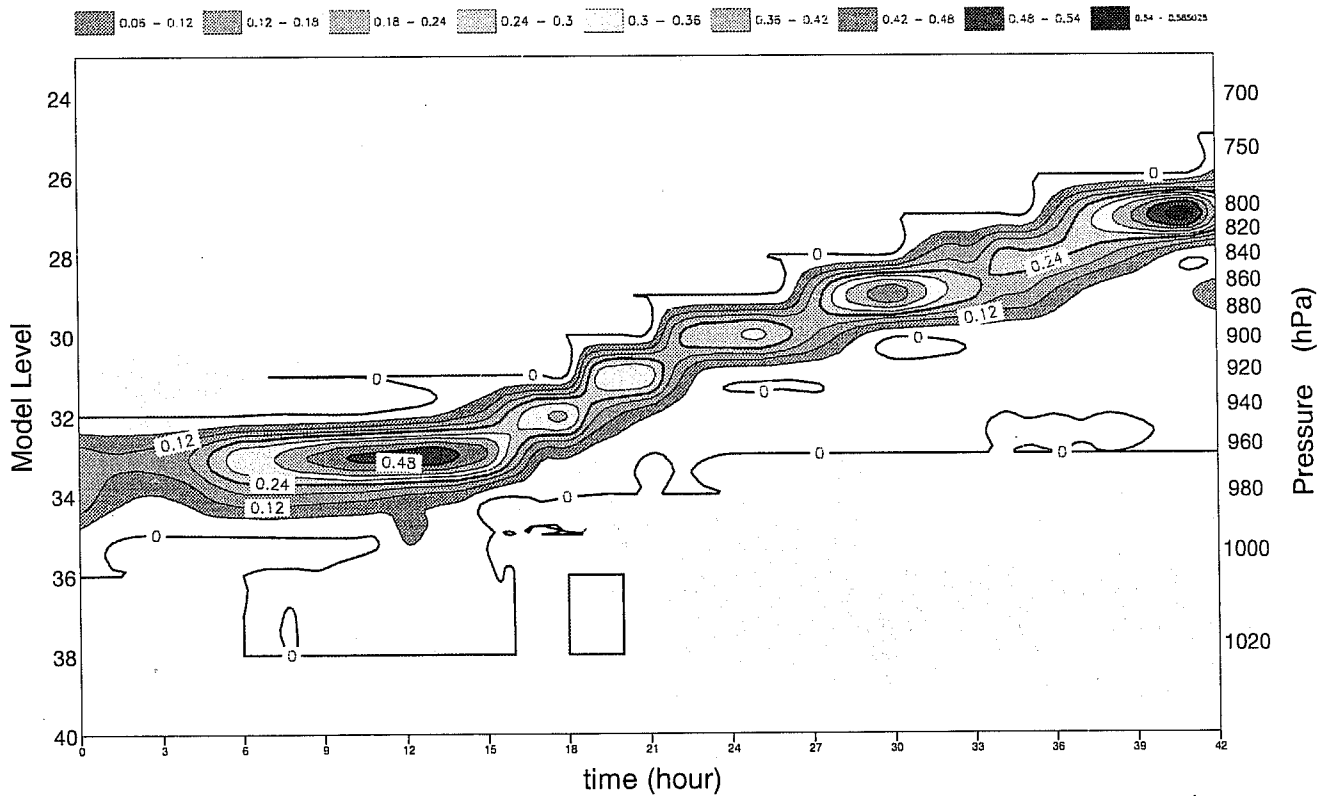
Fig. 8   The same as in fig.7 but for the L40 model.
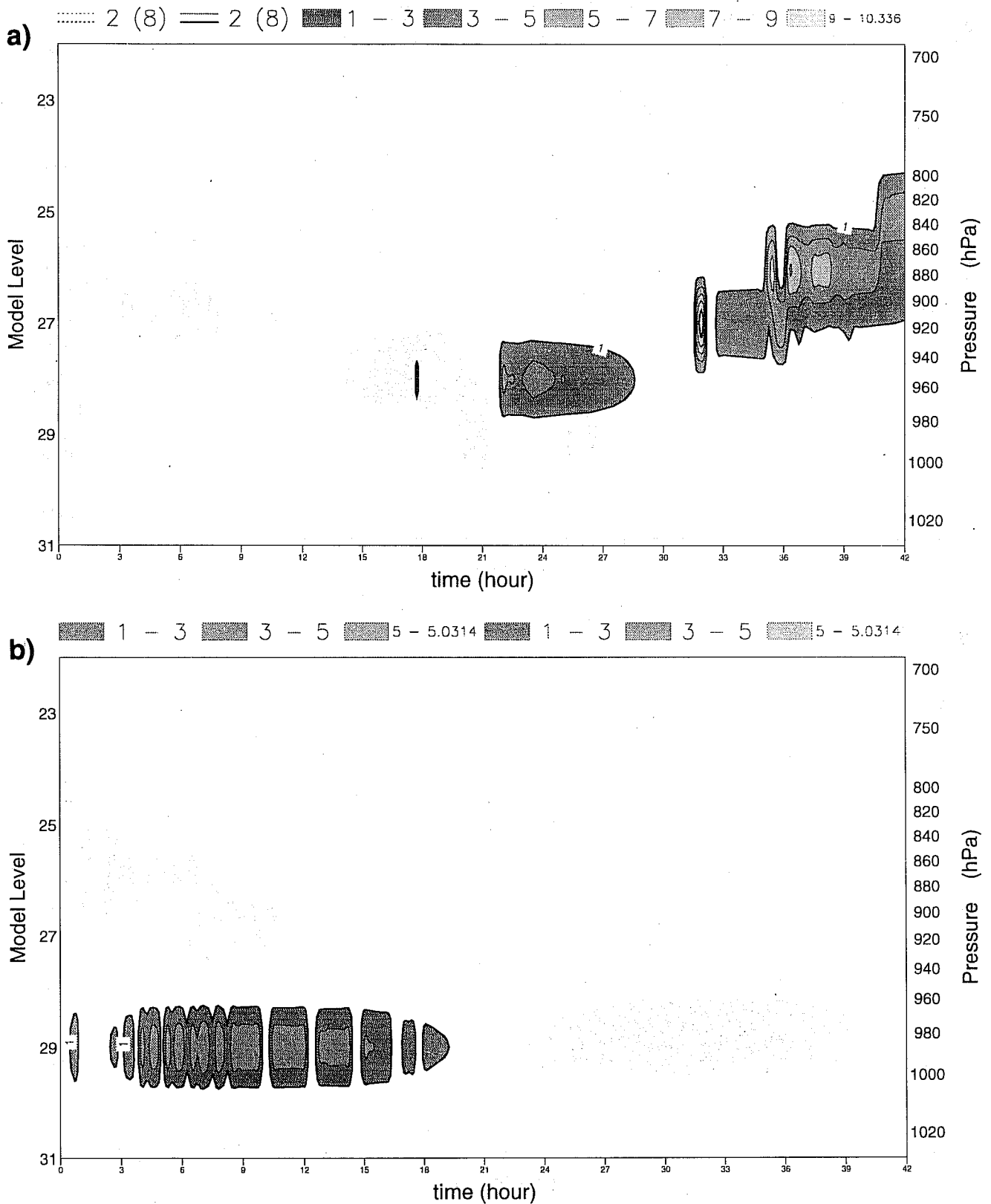
Fig. 9 (a-d) The evolution of the following terms of the liquid water equation for the L31 model: (a) the production of liquid water due to detrainment from convection, (b) the production of liquid water due to large-scale condensation,

c)

d)
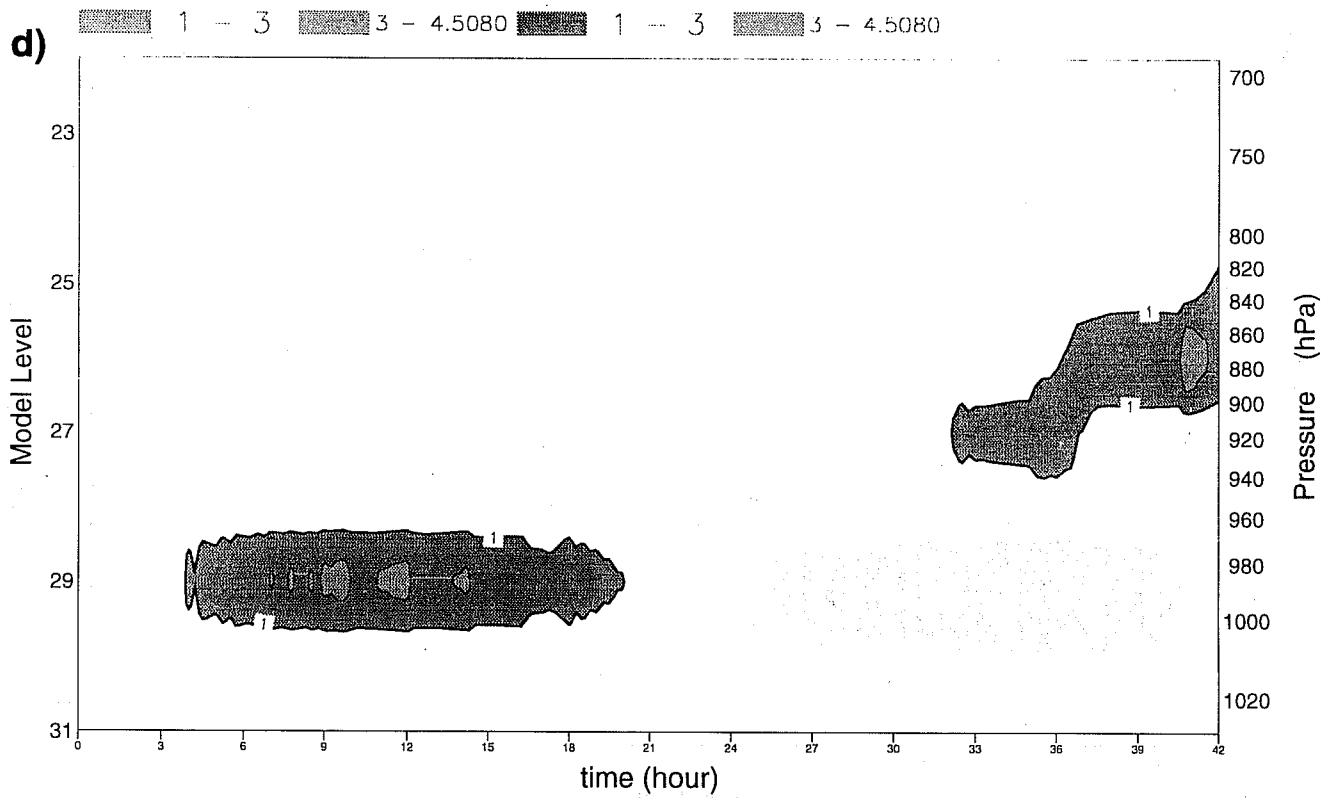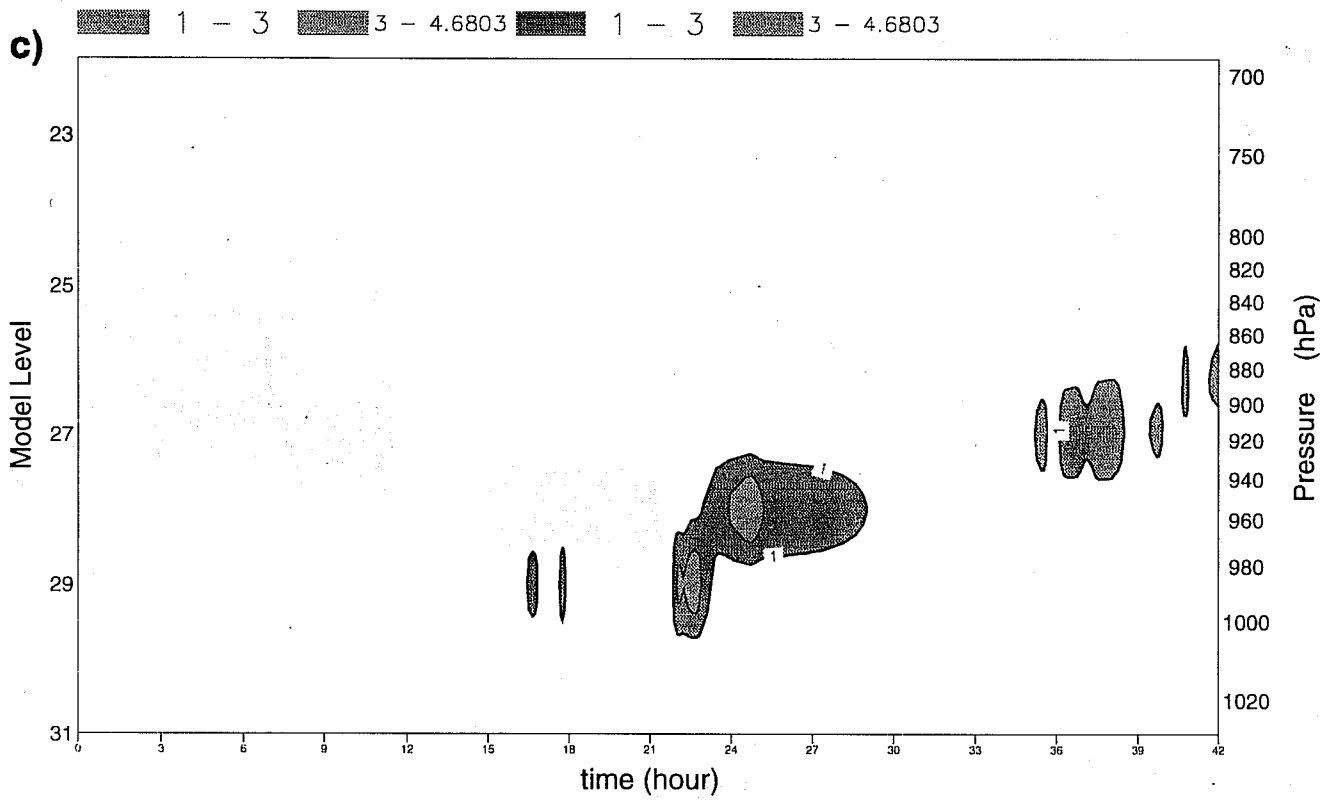
Fig. 9 (Cont) (c) the destruction of liquid water due to large-scale evaporation and (d) the destruction of liquid water due to the conversion of water into rain. The units are in g/kg/day.
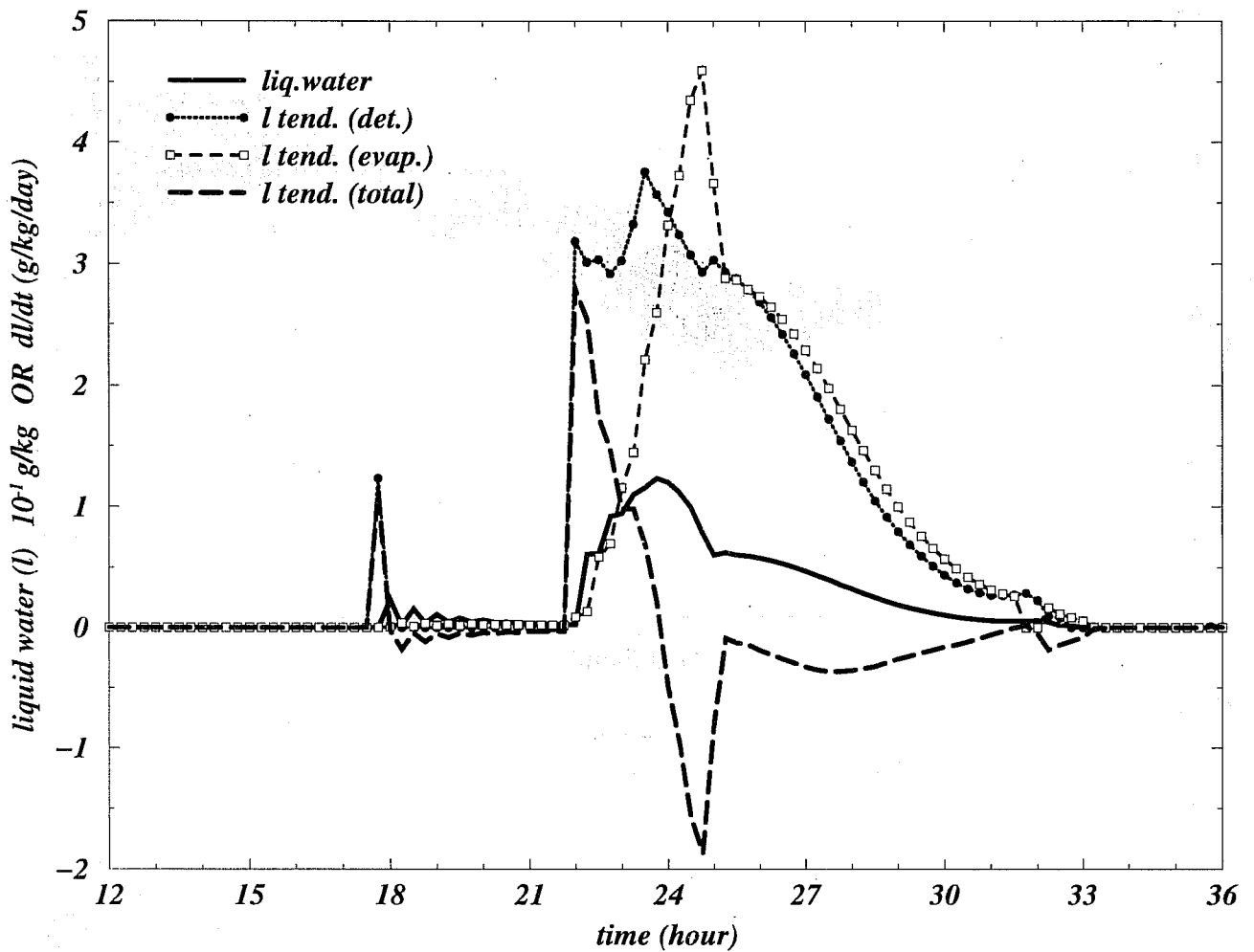
Fig. 10 The liquid water evolution at level 28 (in 10g/kg), the total liquid water tendency and the detrainment and evaporation tendencies (all in g/kg/day).

a)

b)
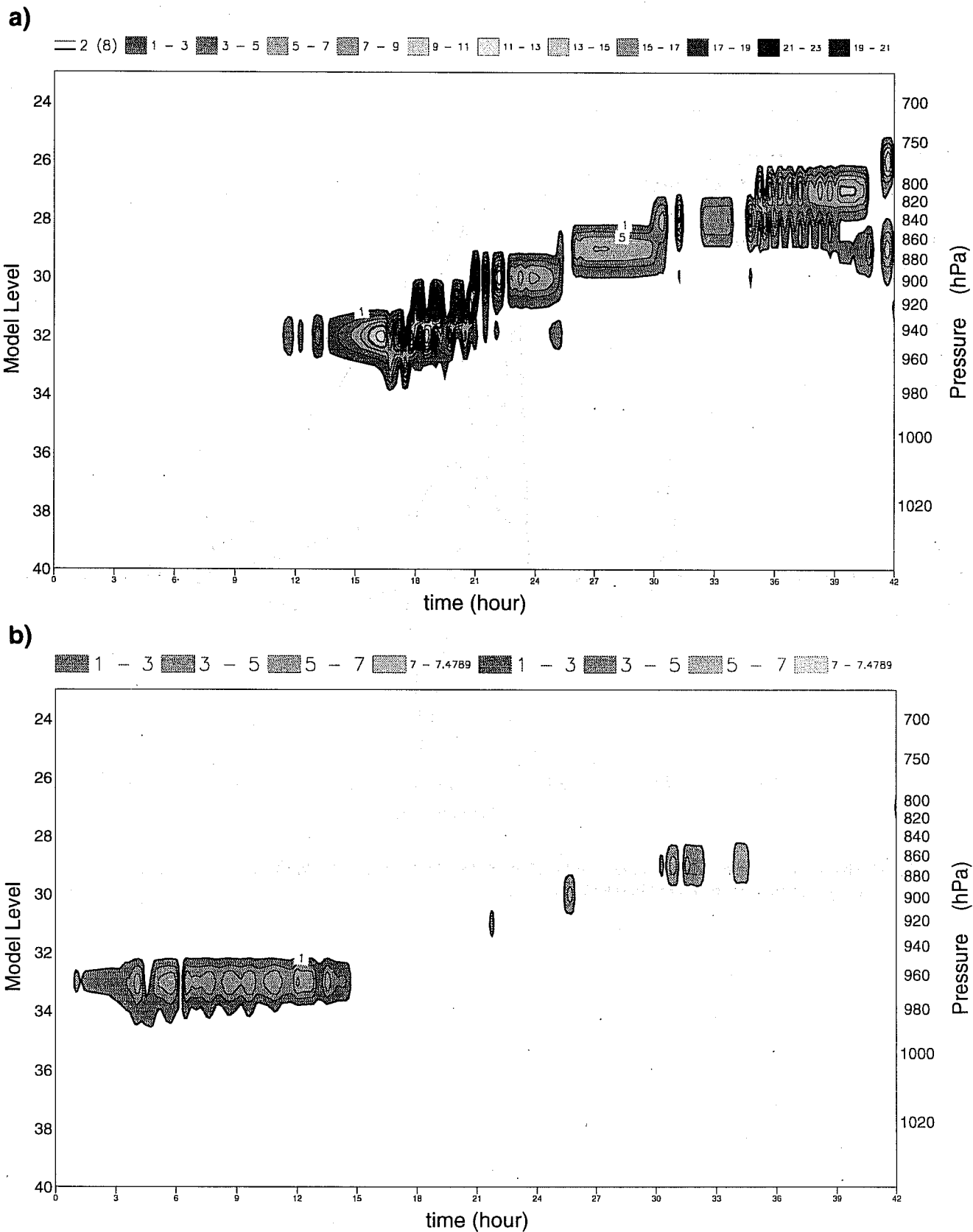
Fig. 11 (a-d) The same as in fig.9 but for the 40 level model.

c)

d)
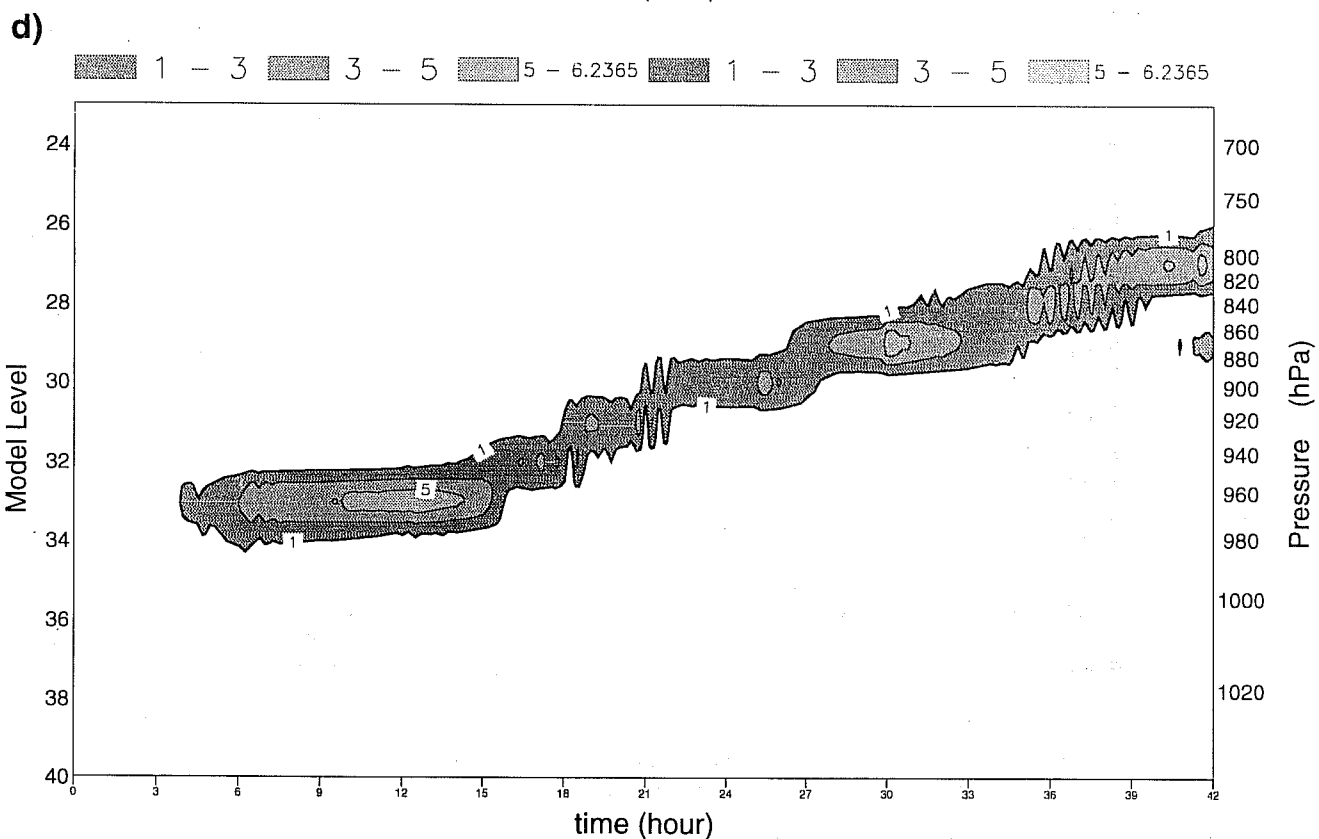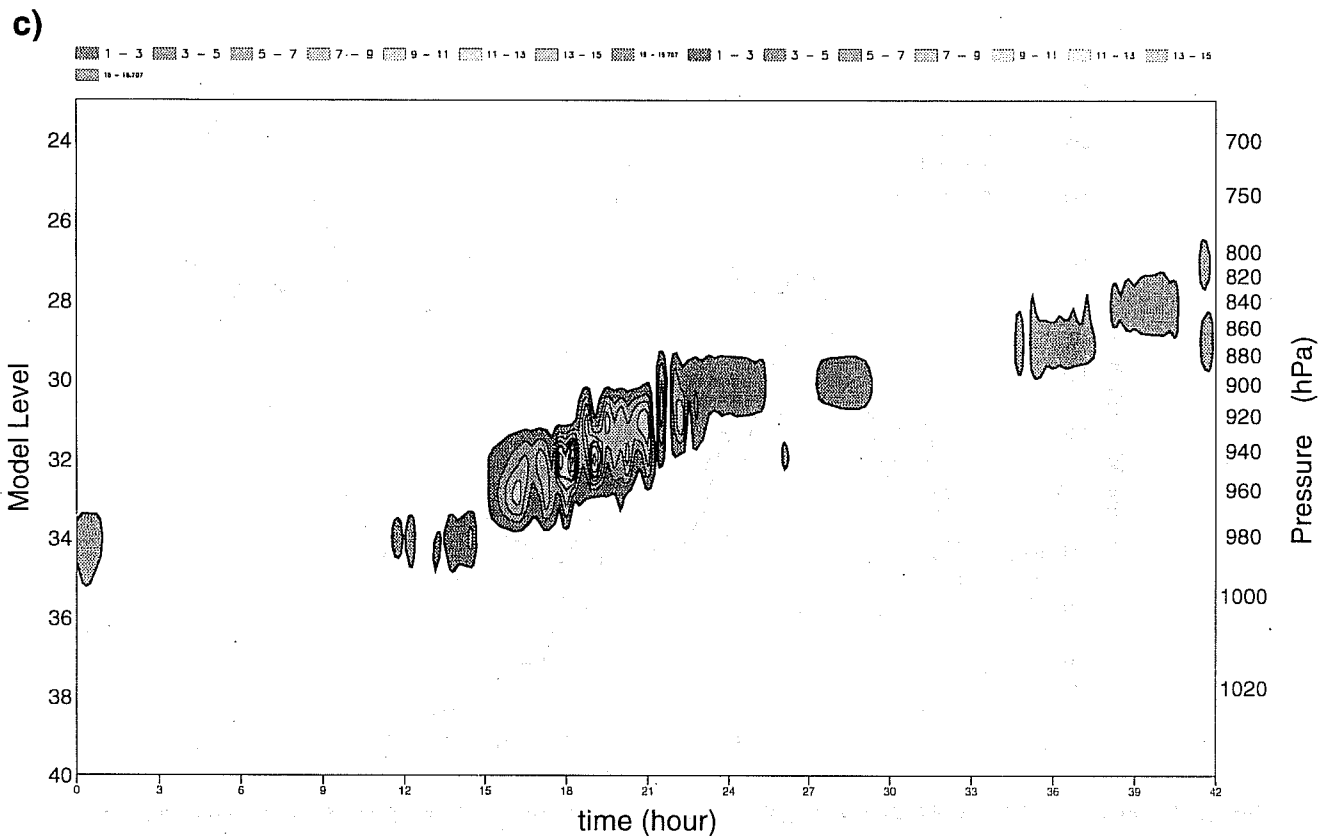
Fig. 11 (Cont)

Fig. 12 The evolution of the Liquid Water Path (LWP) for the observations, the L31 model and the L40 model (in g/m^2).
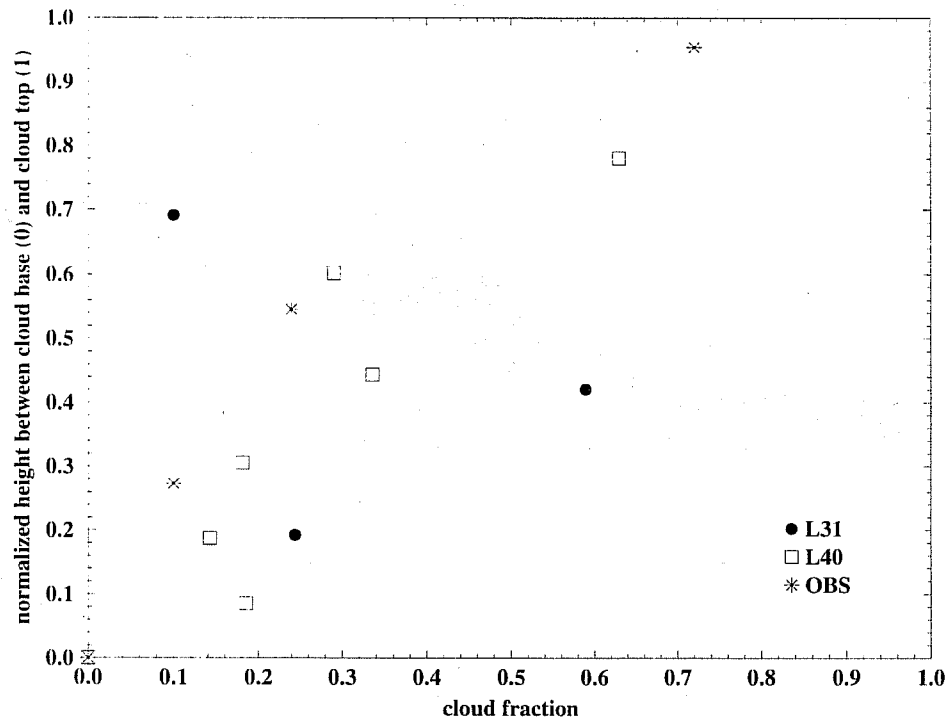
Fig. 13   The cloud fraction vertical structure, at the end of the simulation period, for both models and the observations, versus a normalized height between the cloud base and cloud top (see text for details).

a)
[:·:] 20 – 40 [▨] 40 – 60 [▩] 60 – 80 [▨] 80 – 100

b)
[■] -99.612 – -70 [░] -70 – -40 [■] -40 – -10 [:·:] 10 – 40 [▩] 40 – 70 [▨] 70 – 100

c)
[■] -91.355 – -70 [░] -70 – -40 [■] -40 – -10 [:·:] 10 – 40 [▩] 40 – 70 [▨] 70 – 100
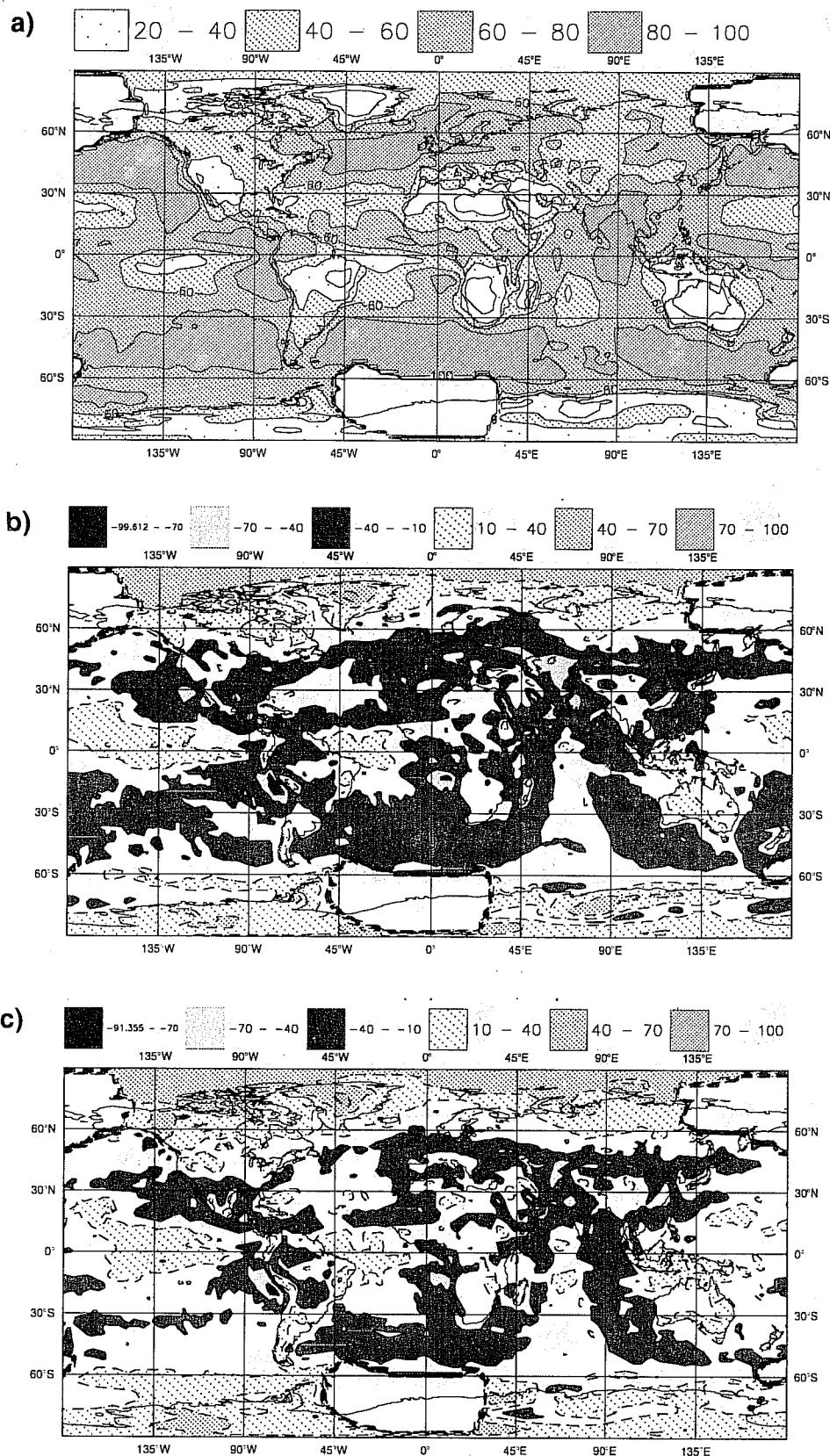
Fig. 14 (a) the global distribution of the mean cloud cover, in %, according to the International Satellite Cloud Climatology Project (ISCCP) for the period JJA 1987. (b) and (c) are, respectively, the differences between the L31 mean cloud cover and ISCCP and the L40 mean cloud cover and the ISCCP data, for the same period.

a)

b)

c)
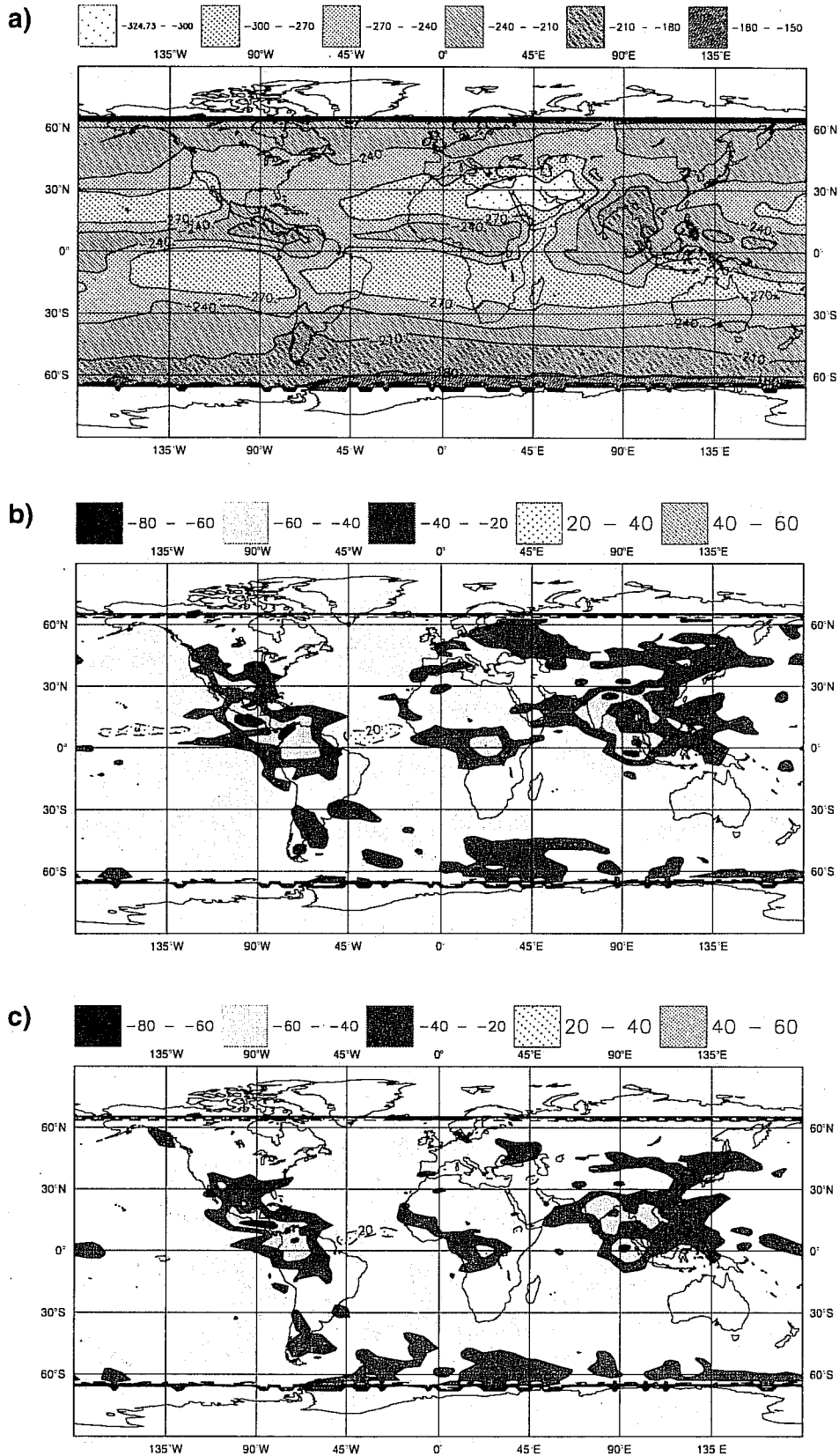
Fig. 15 (a) the global distribution of Outgoing Longwave Radiation (OLR), in Wm^{-2}, as estimated by the Earth Radiation Budget Experiment (ERBE) for the period JJA 87. (b) and (c) are respectively the OLR differences between the L31 model and ERBE and between the L40 model and ERBE.

a)

b)

c)
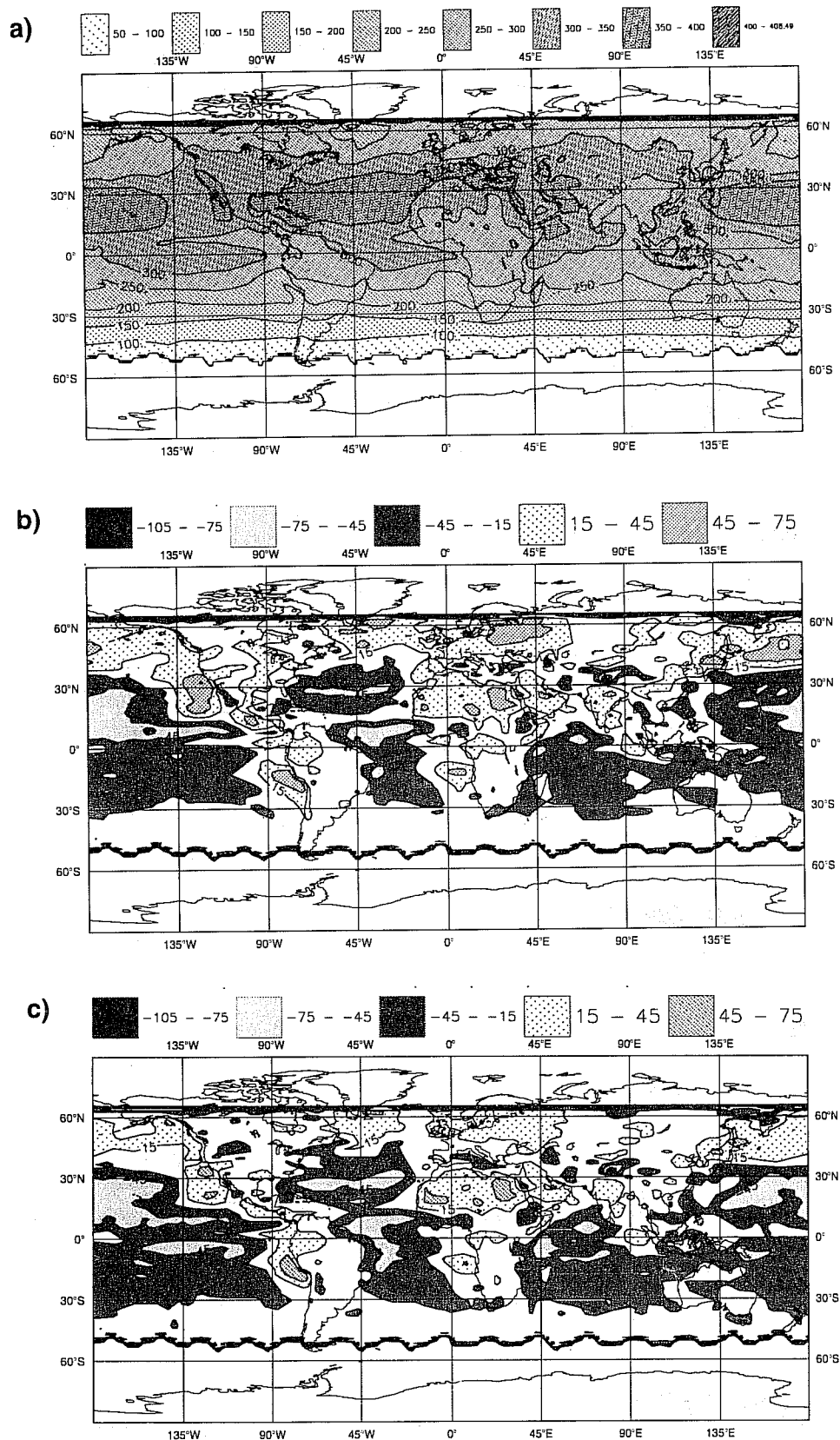
Fig. 16 (a) the global distribution of Top Shortwave Radiation (TSR), in Wm⁻², as measured by ERBE for the period JJA 87. (b) and (c) are respectively the TSR differences between the L31 model and ERBE and between the L40 model and ERBE.

a)

b)

c)
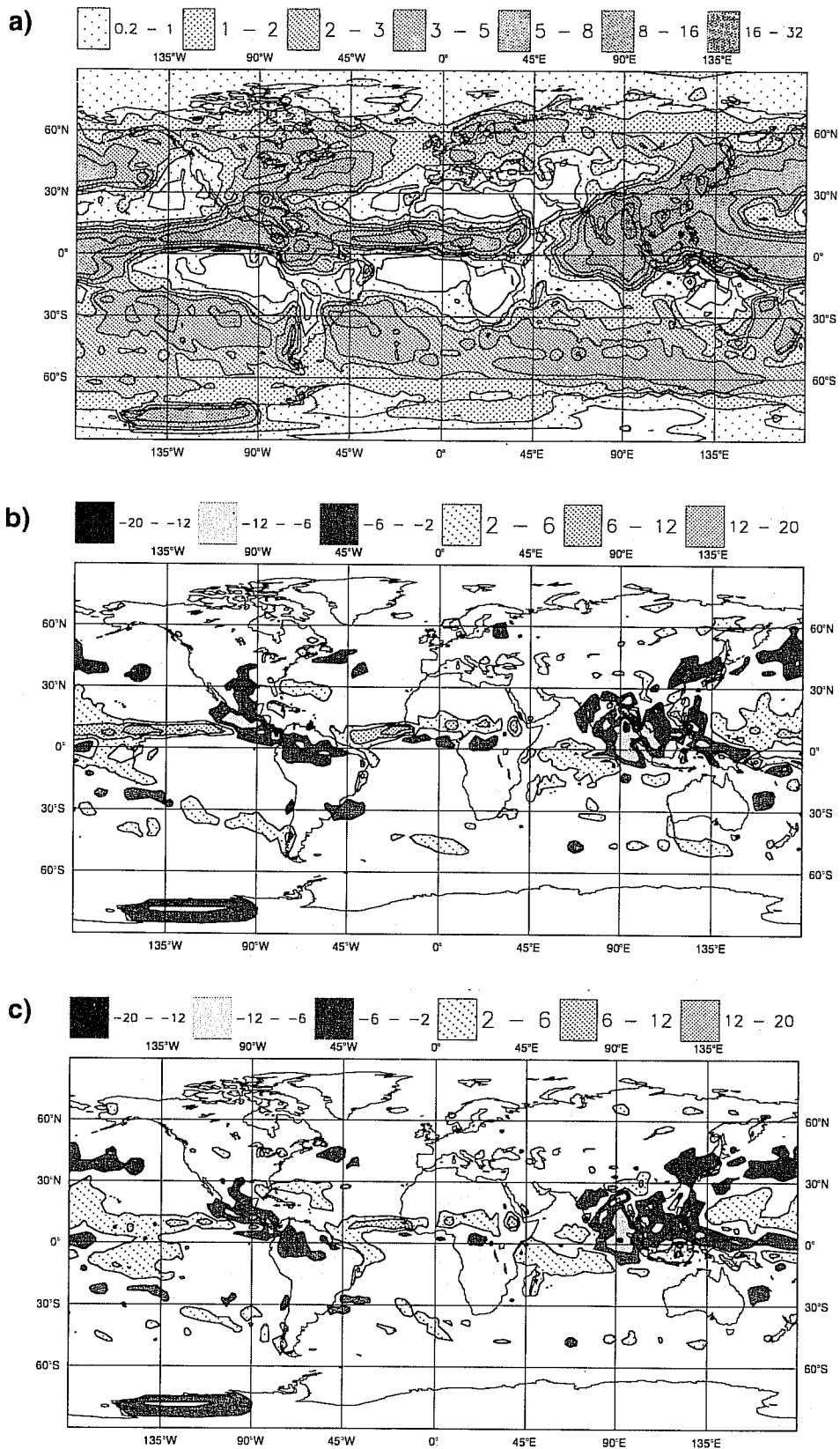
Fig. 17 (a) the global distribution of precipitation, in mm/day, as estimated by the Global Precipitation Climatology Project (GPCP) for the period JJA 87. (b) and (c) are respectively the precipitation differences between the L31 model and GPCP and between the L40 model and GPCP.

a)

b)

c)
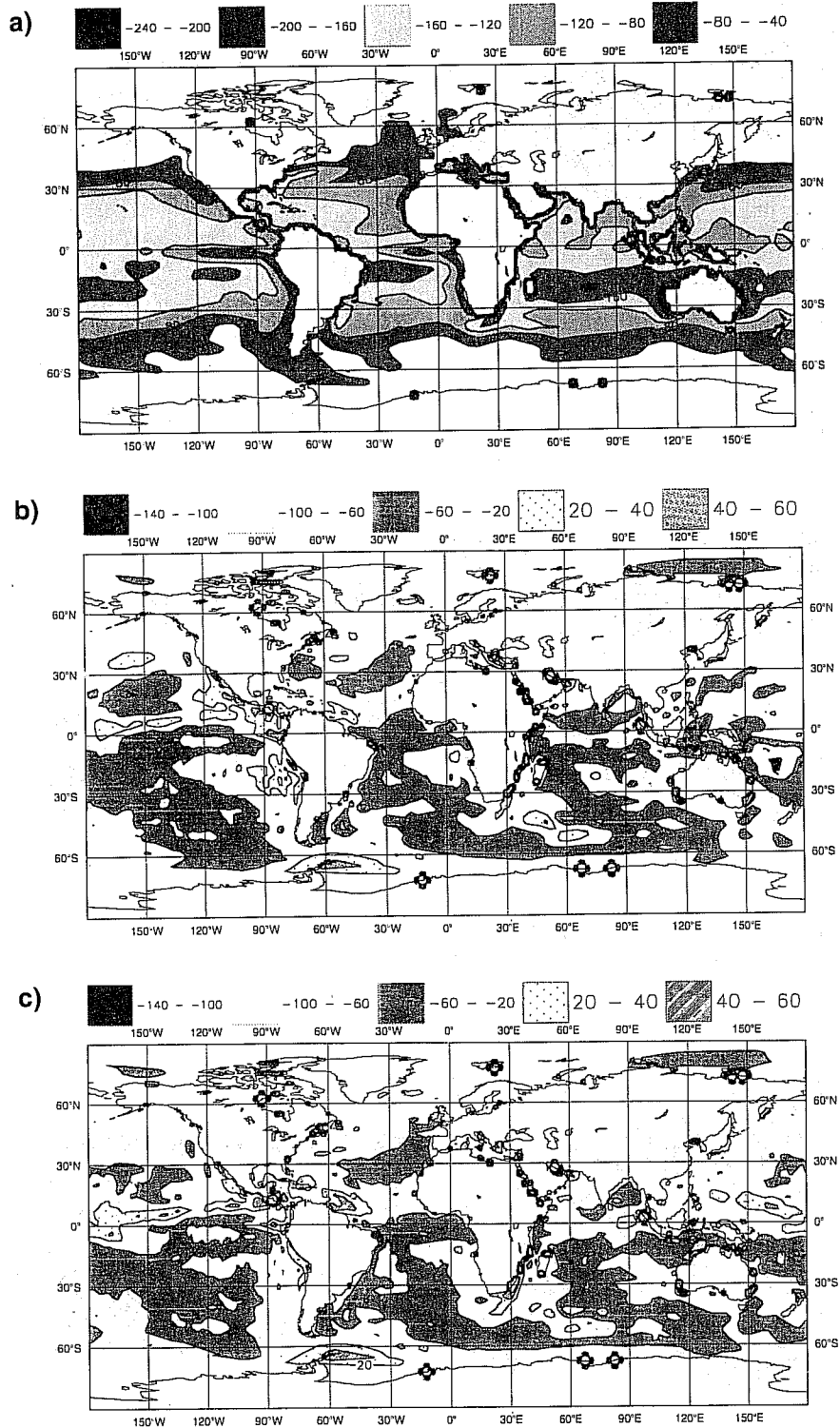
Fig. 18 (a) the global distribution of the Surface Latent Heat Flux (SLHF), in Wm⁻², as given by the climatology of Silva et al. (1994) for JJA 87. This climatology is based on individual observations that are part of the Comprehensive Ocean-Atmosphere Data Set (COADS) from January 1945 to December 1989. Negative values in the surface fluxes correspond to heat being transferred from the ocean to the atmosphere which leads to a cooling of the ocean surface. Positive values correspond to a warming of the ocean surface. (b) and (c) are respectively the SLHF differences between the L31 model and the climatology and the L40 model and the climatology.

a)

b)

c)
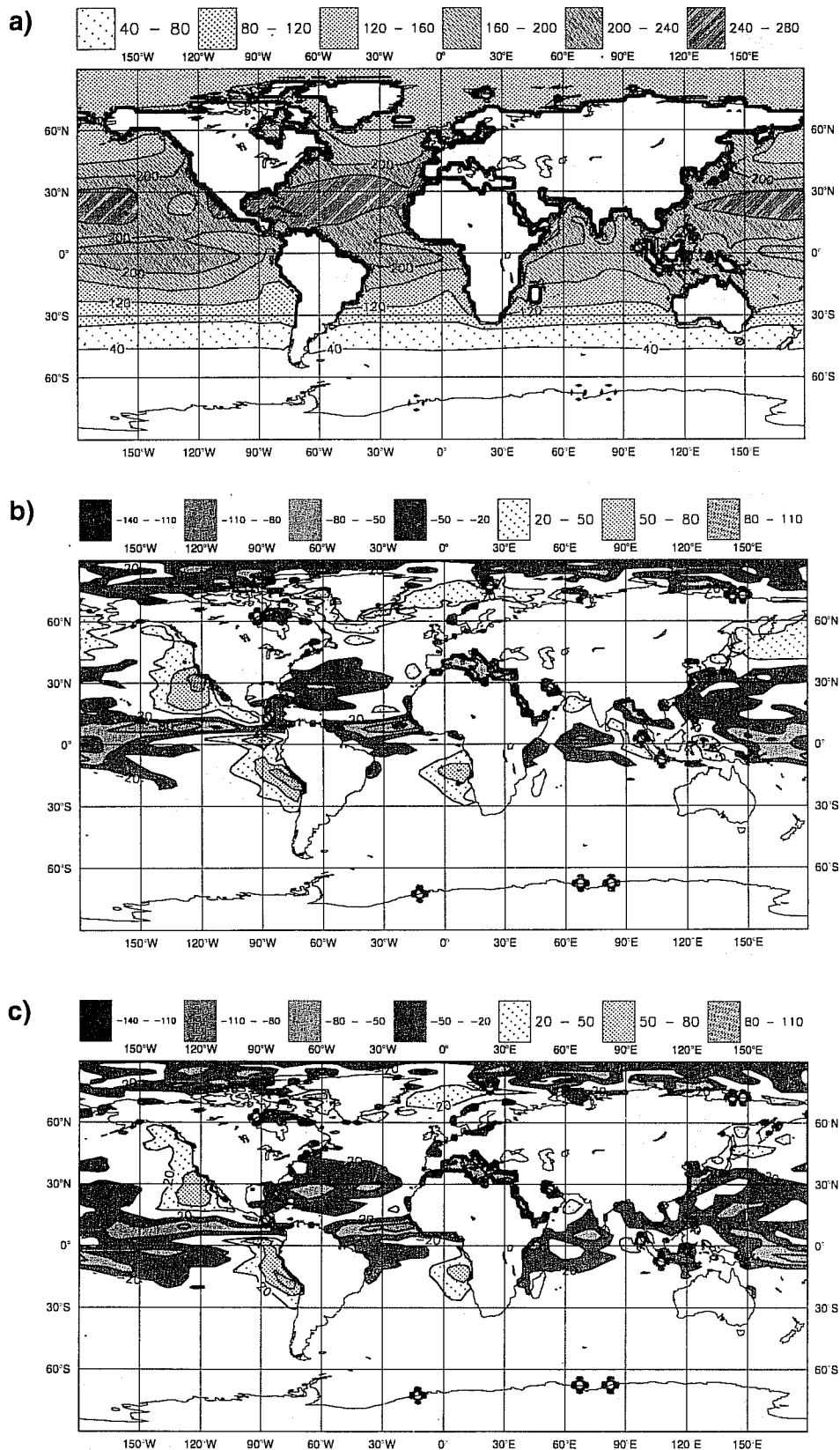
Fig. 19 (a) the global distribution of Surface Shortwave Radiation (SSR), in Wm-2, as given by the climatology of Silva (1994) for JJA 87. (b) and (c) are respectively the SSR differences between the L31 model and climatology and the L40 model and the climatology.
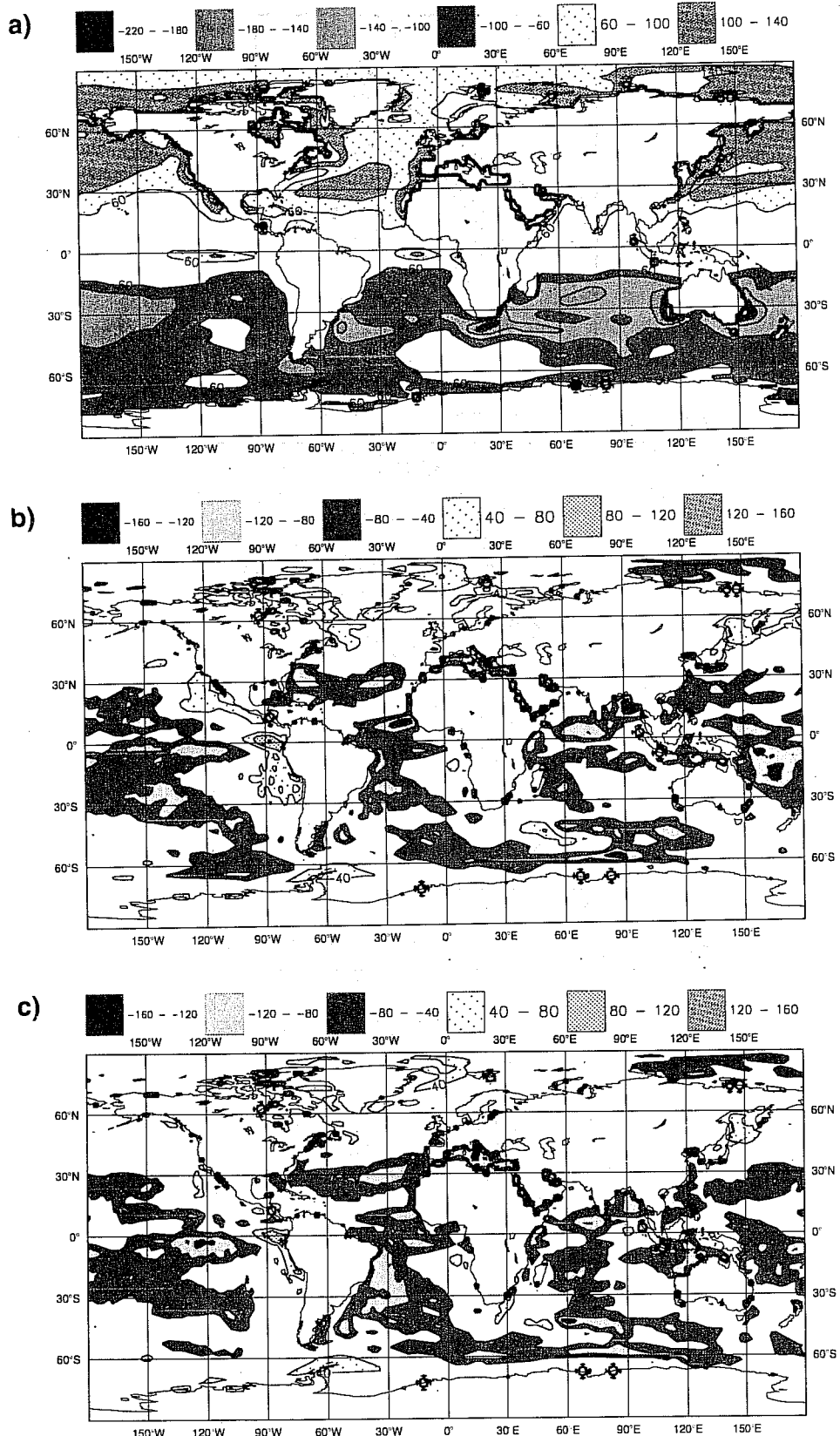
Fig. 20 (a) the global distribution of the Net Surface Flux (NSF), in Wm^{-2}, as given by the climatology of Silva (1994) for JJA 87. (b) and (c) are respectively the NSF differences between the L31 model and the climatology and the L40 model and the climatology.

a)

b)

c)
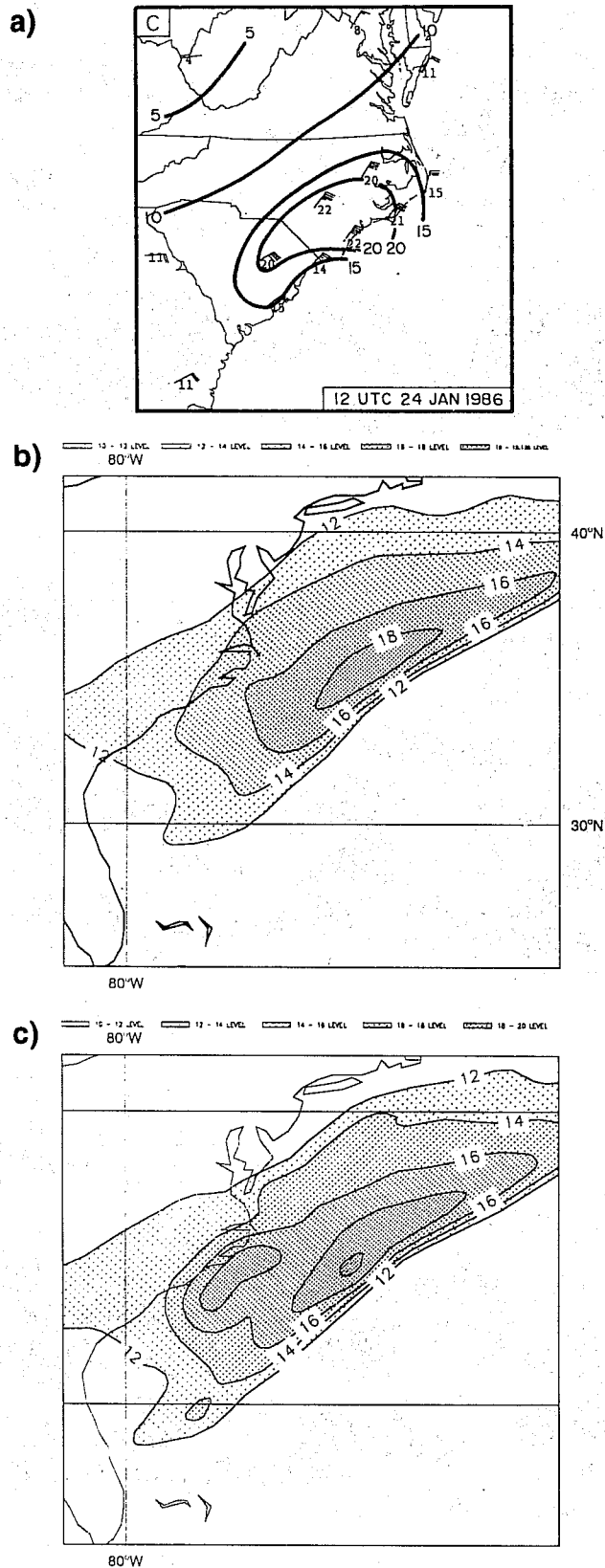
Fig. 21 Wind speed, in m/s, contours for (a) a low-level jet observed, at the 960 hPa level, along the U.S. East Coast using special observing data taken during the Genesis of Atlantic Lows Experiment (GALE), (b) a 24 hour forecast, at around 970 hPa, with the L31 model and (c) with the L40 model.
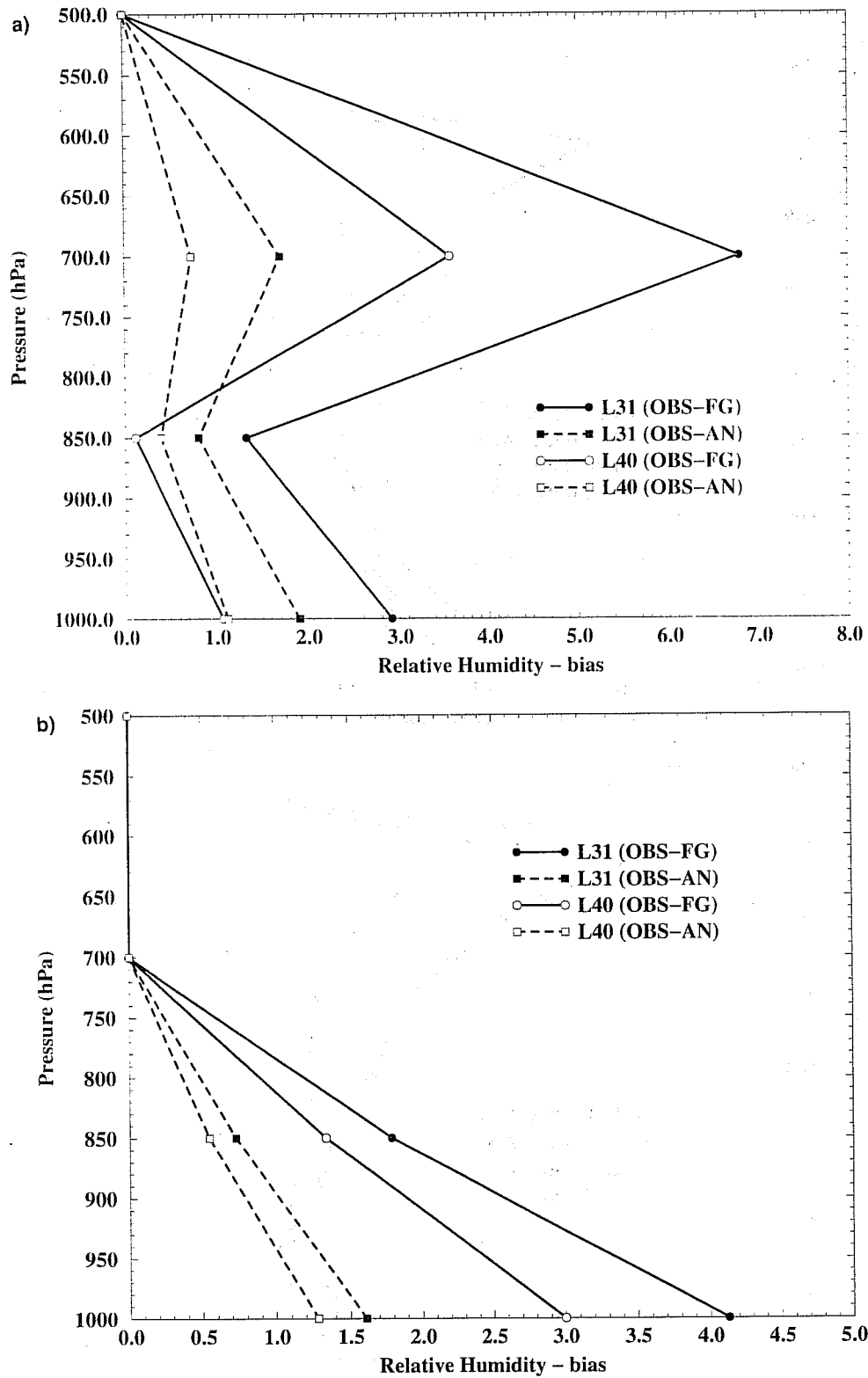
Fig. 22 The relative humidity bias in terms of SYNOP observations minus first guess (OBS-FG) and minus analysis (OBS-AN) for (a) the Tropics and (b) the Southern Hemisphere. The data analysed corresponds to 14 days (00 UTC and 12 UTC) of the 3D-Var summer assimilation experiment. The values at 1000 hPa correspond to the layer of 1000-850 hPa, the ones at 850 hPa to 850-700 hPa, the ones at 700 hPa to 700-500 hPa and the ones at 500 hPa to 500-400 hPa.
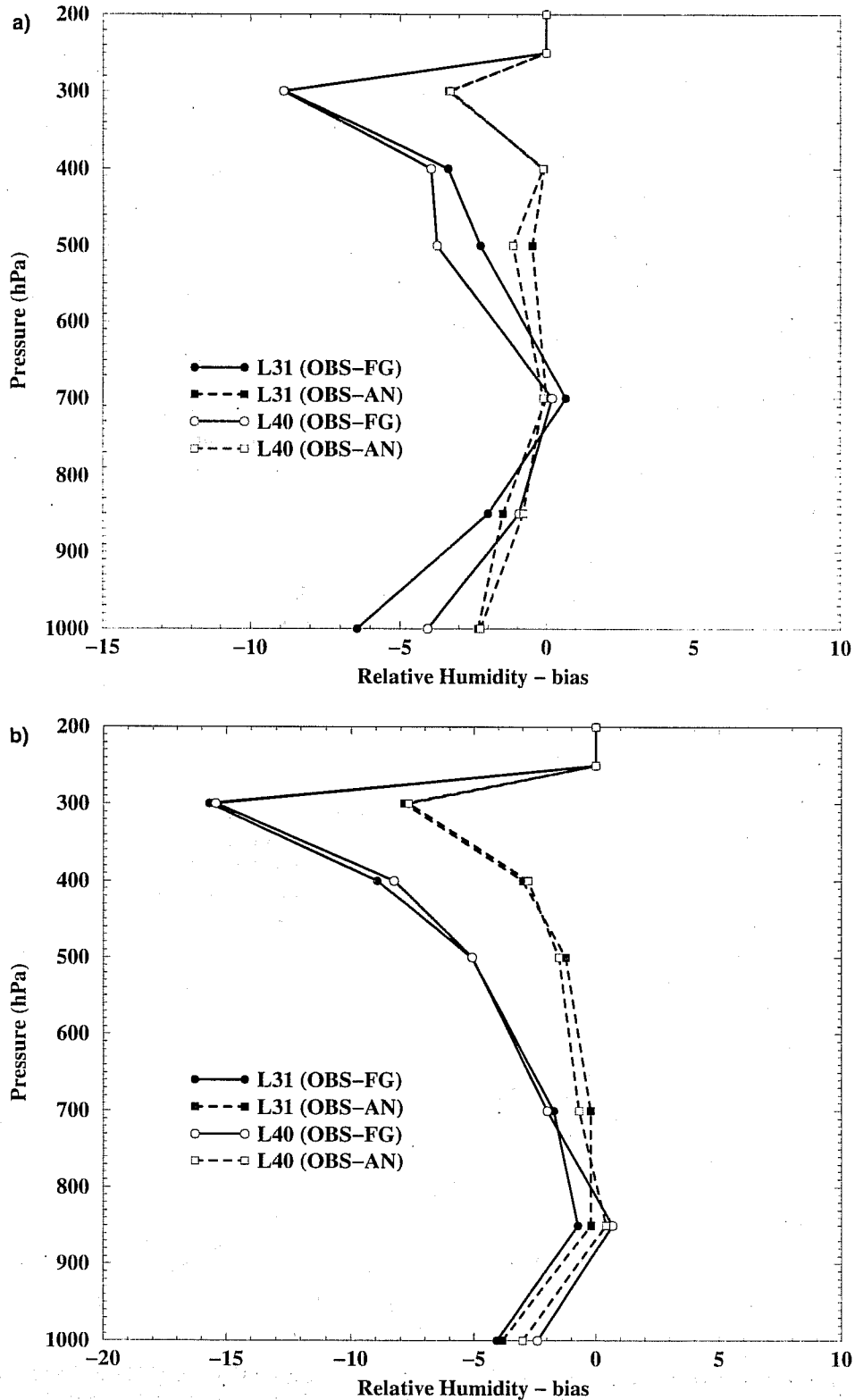
Fig. 23 The same as in fig. 22 is shown, but for the TEMP observations. In this case also included are values at 400 hPA which corresponds to the layer 400-300 hPa, 300 hPa that corresponds to 300-250 hPa, 250 hPa that corresponds to 250-200 hPa and 200 hPa that corresponds to 200-150 hPa.
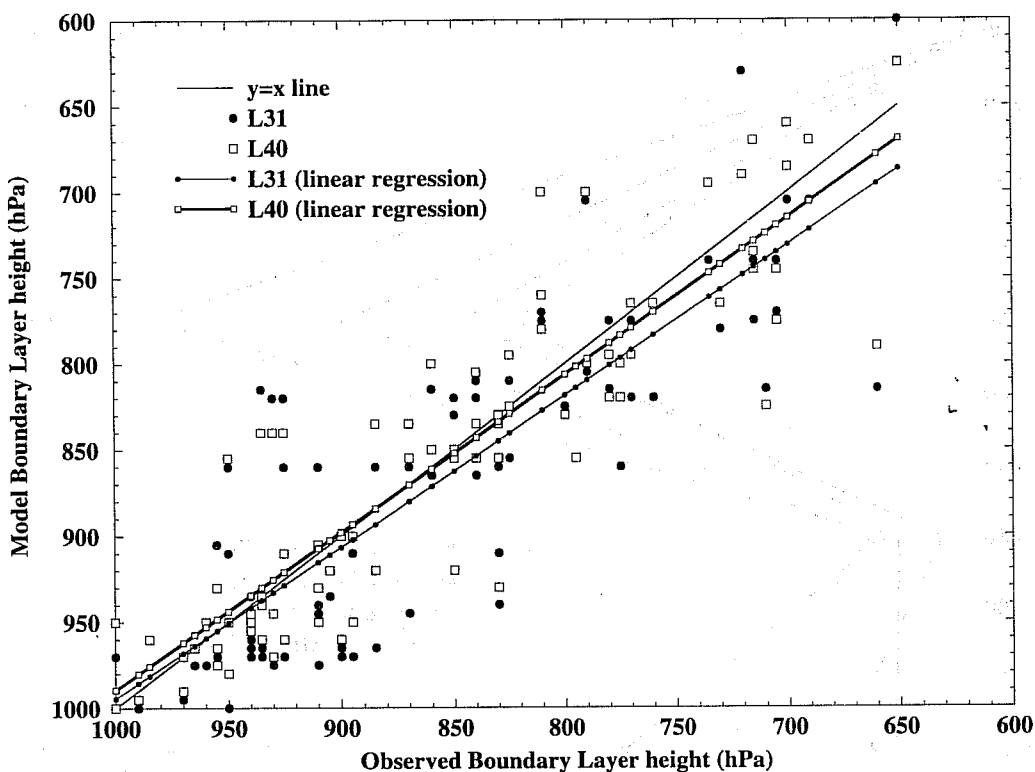
Fig. 24 Scatter plot of the observed versus the model (L31 and L40 24 h forecasts) inversion height.
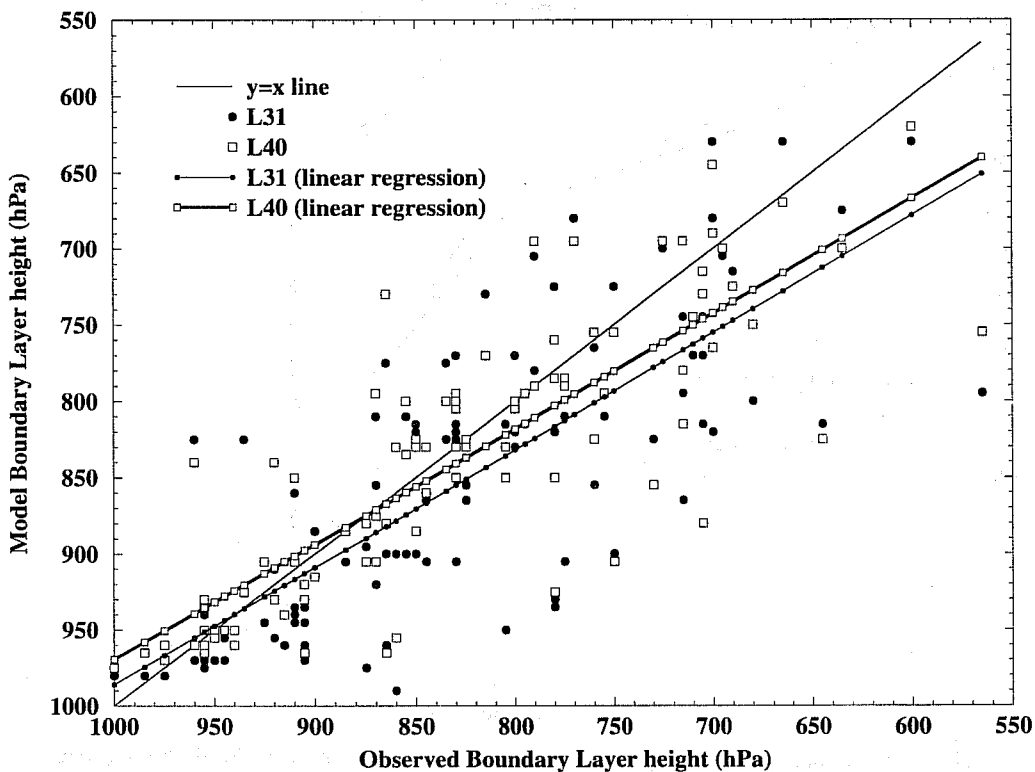
Fig. 25 The same as in fig.24 but for 120 h forecasts.
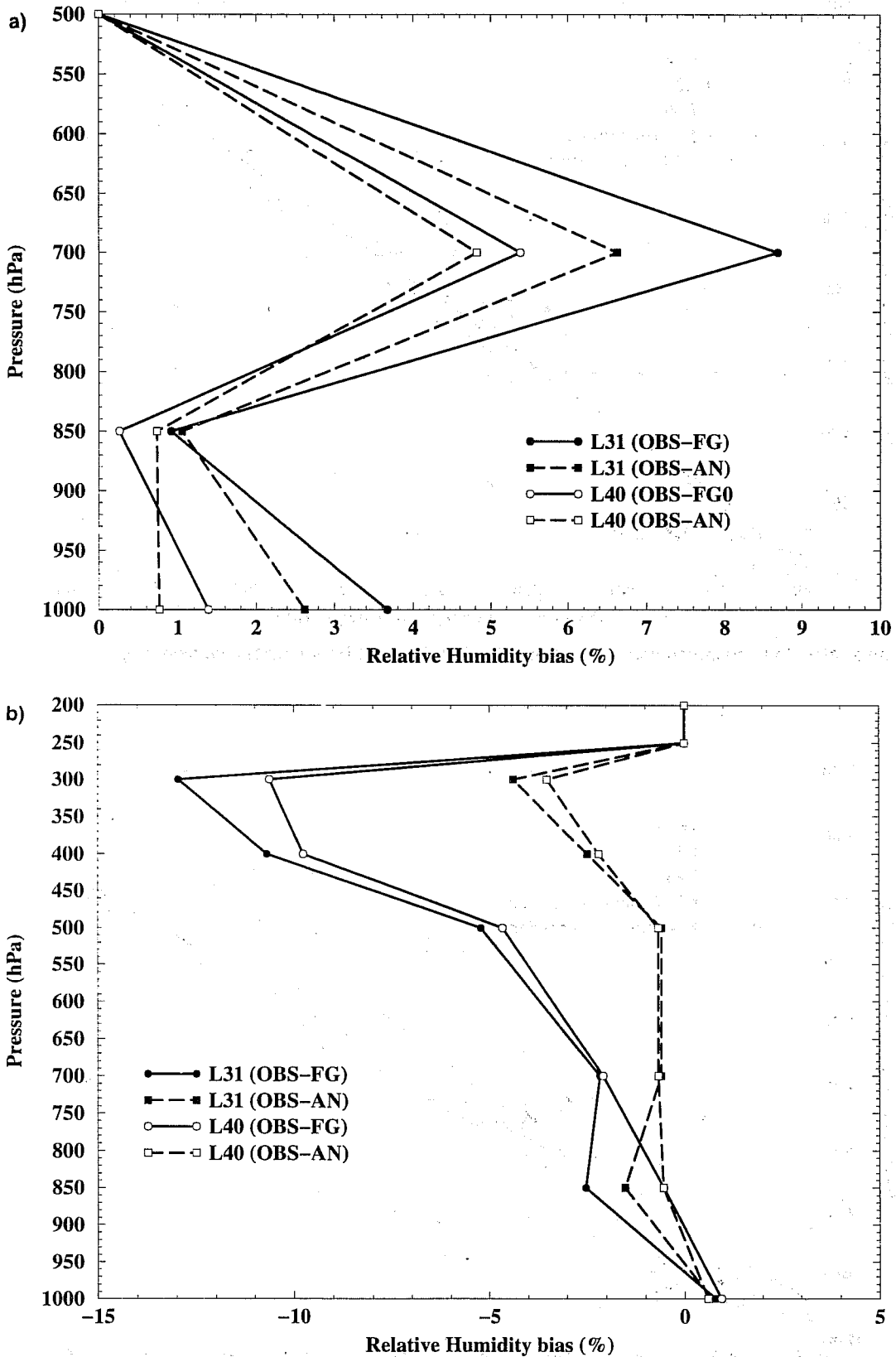
Fig. 26 The relative humidity bias, for the Tropics, in terms of (a) SYNOP and (b) TEMP observations. OBS-FG corresponds to observations minus first-guess and (OBS-AN) to observations minus analysis. The data analysed corresponds to 14 days (00 UTC and 12 UTC) of the 4D-Var spring assimilation experiment.
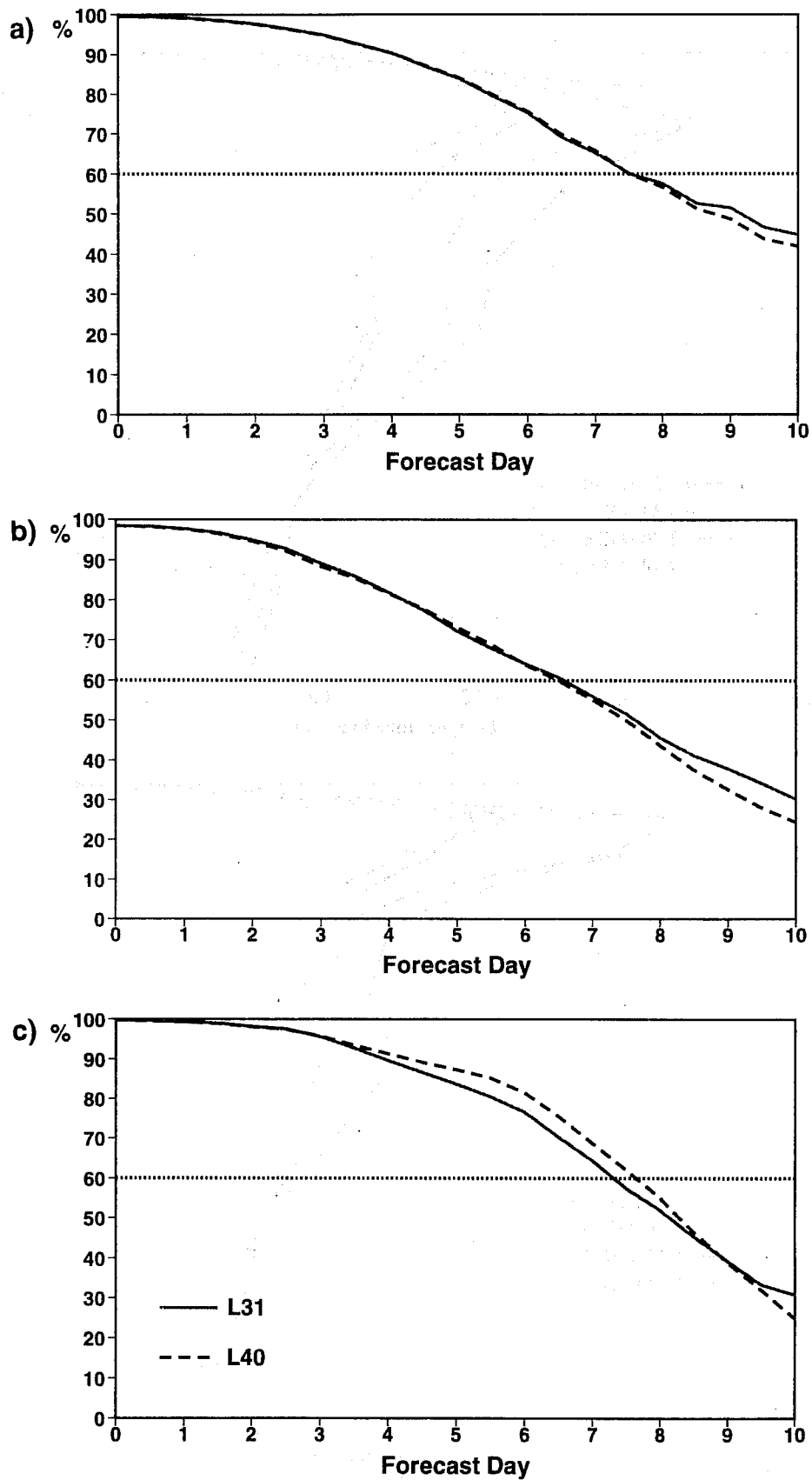
Fig. 28 The anomaly correlation 500 hPa geopotential scores for the 17 spring L40 and L31 forecasts for (a) the Northern Hemisphere, (b) Southern Hemisphere and (c) Europe.
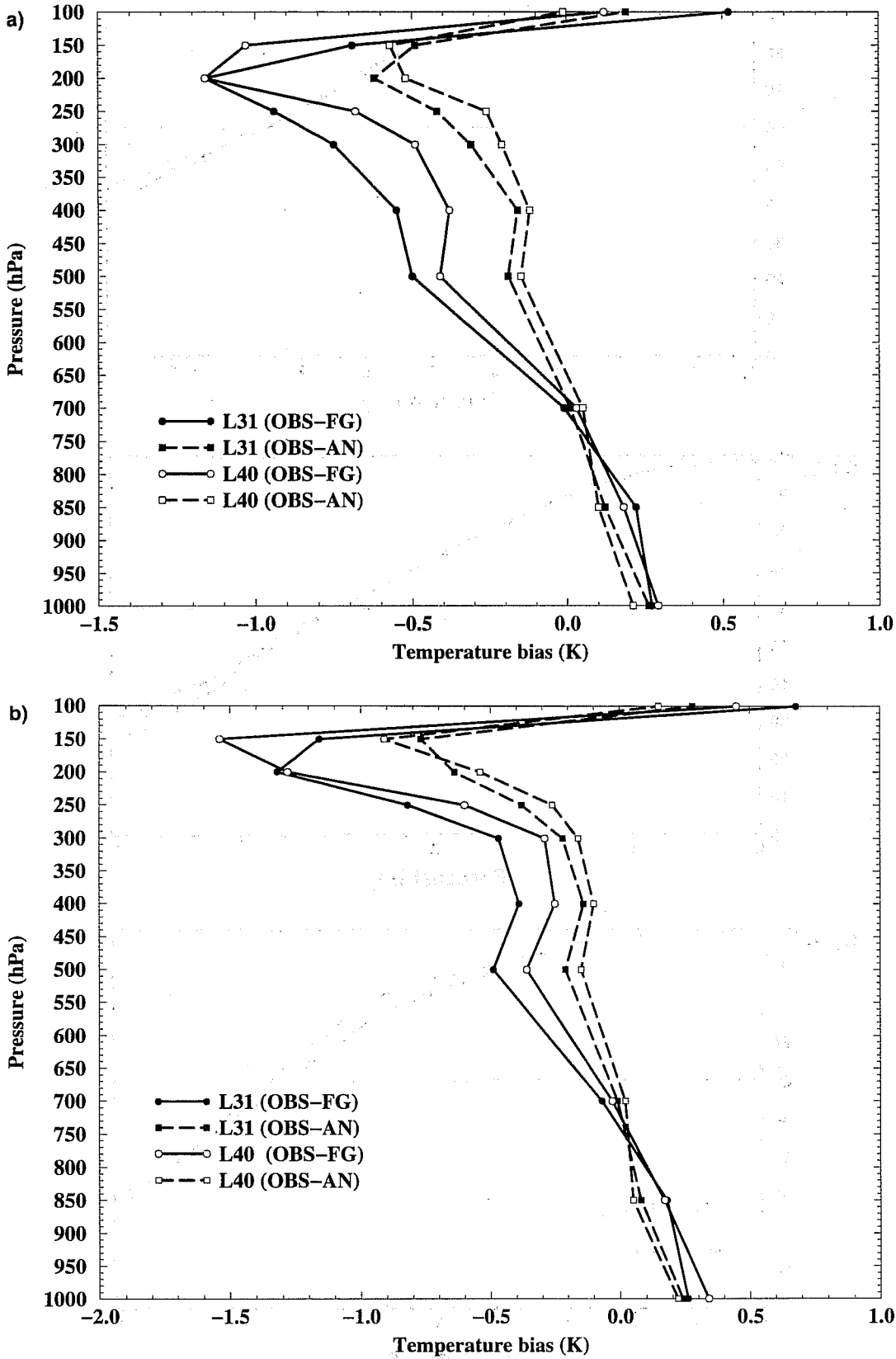
Fig. 27 The temperature bias in terms of tropical TEMP observations minus first guess (OBS-FG) and minus analysis (OBS-AN) for (a) the spring and (b) the winter 4D-Var assimilations (14 days of each experiment).
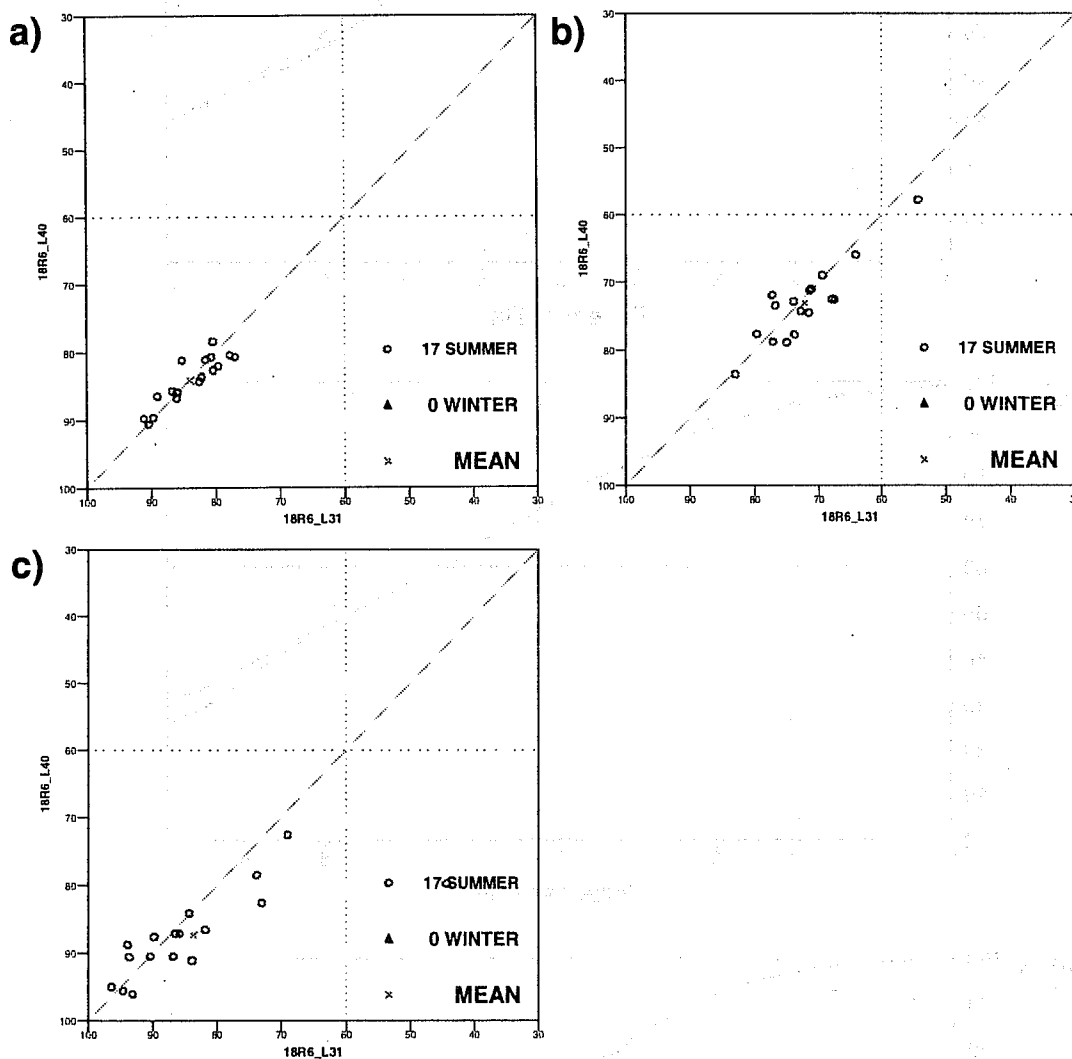
Fig. 29 The scatter plots of the 120h L40 and L31 forecasts for the 500 hPa geopotential anomaly correlation for a) Northern Hemsiphere, b) Southern Hemisphere and c) Europe.
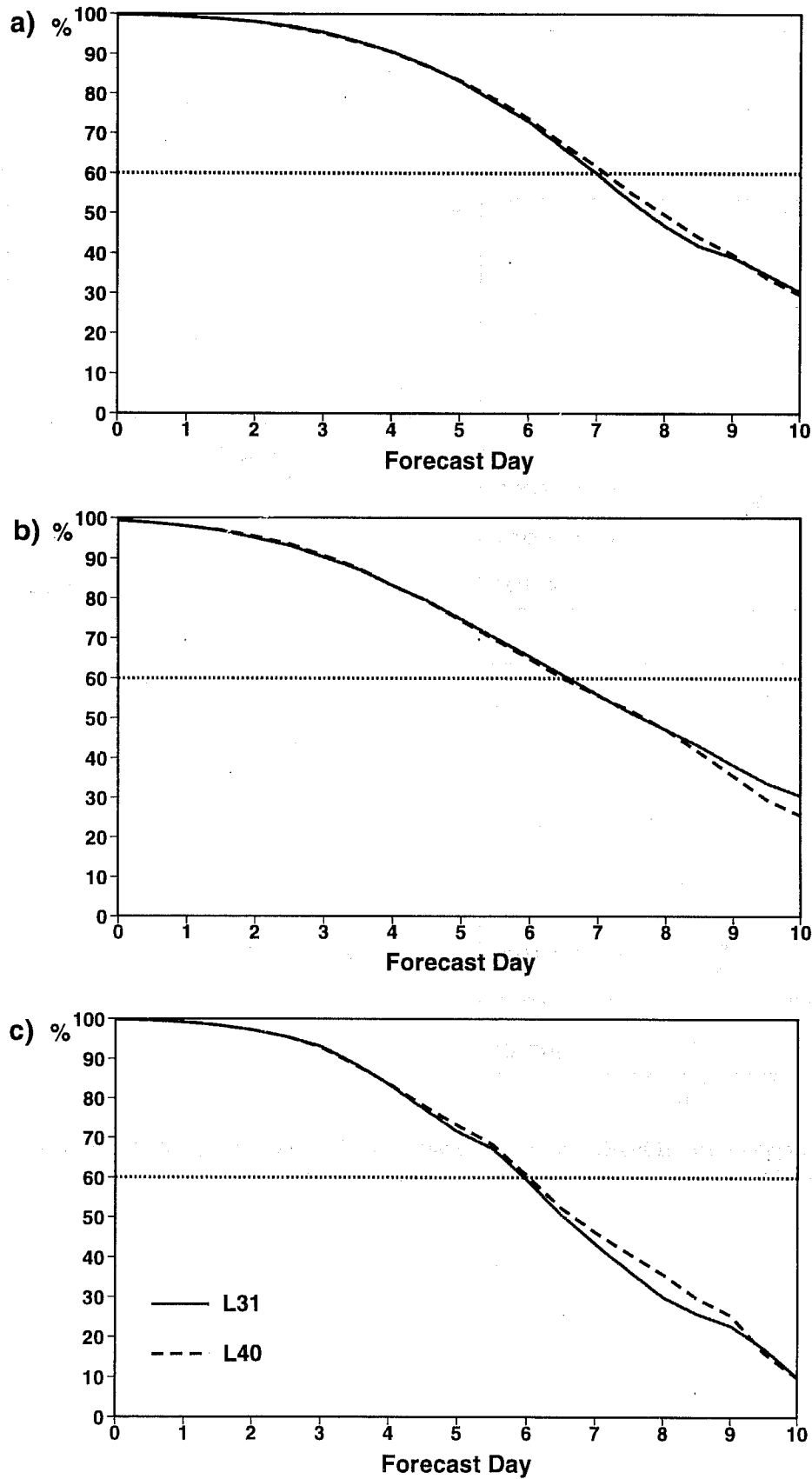
Fig. 30 The 18 winter forecasts scores for the 500 hPa geopotential for the (a) Northern Hemisphere, (b) Southern Hemisphere and (c) Europe.
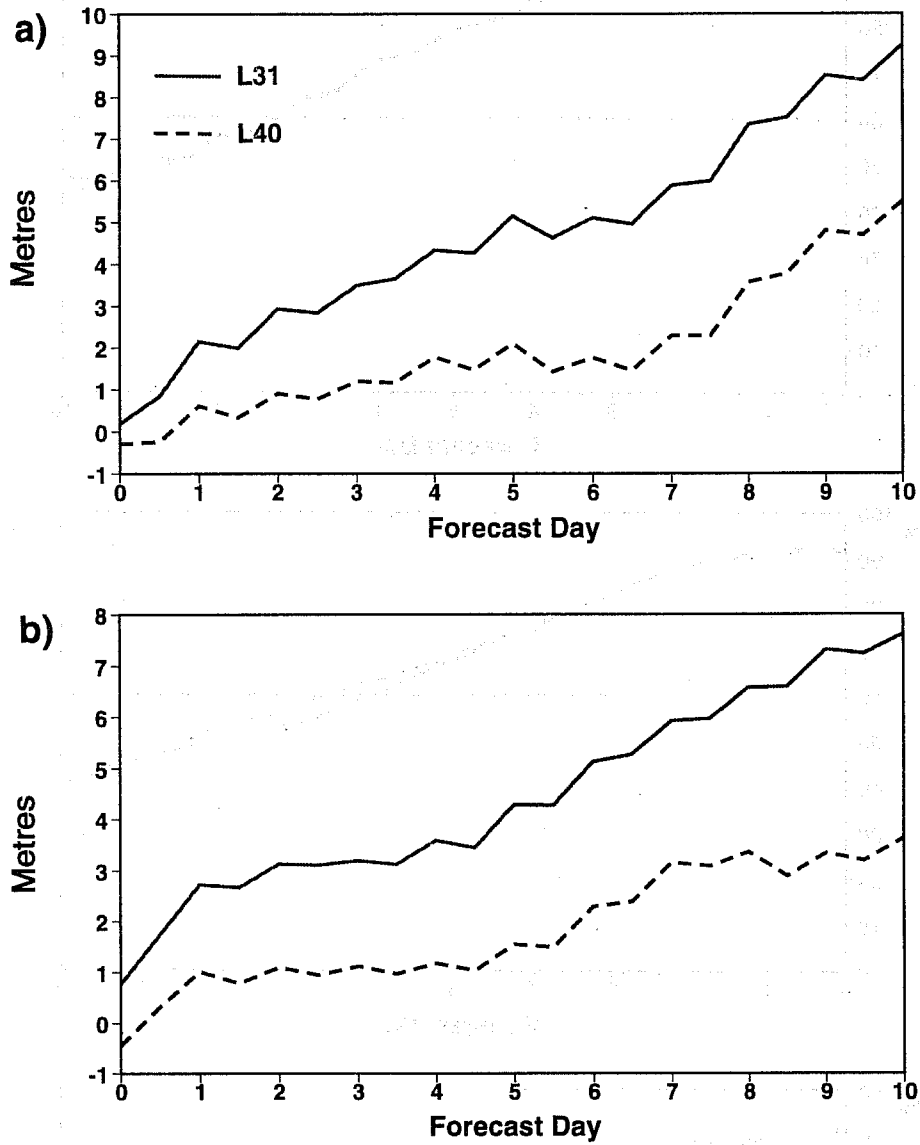
Fig. 31 The 35 (winter and spring) forecasts mean error scores for the 500 hPa geopotential: (a) Northern and (b) Southern Hemisphere.
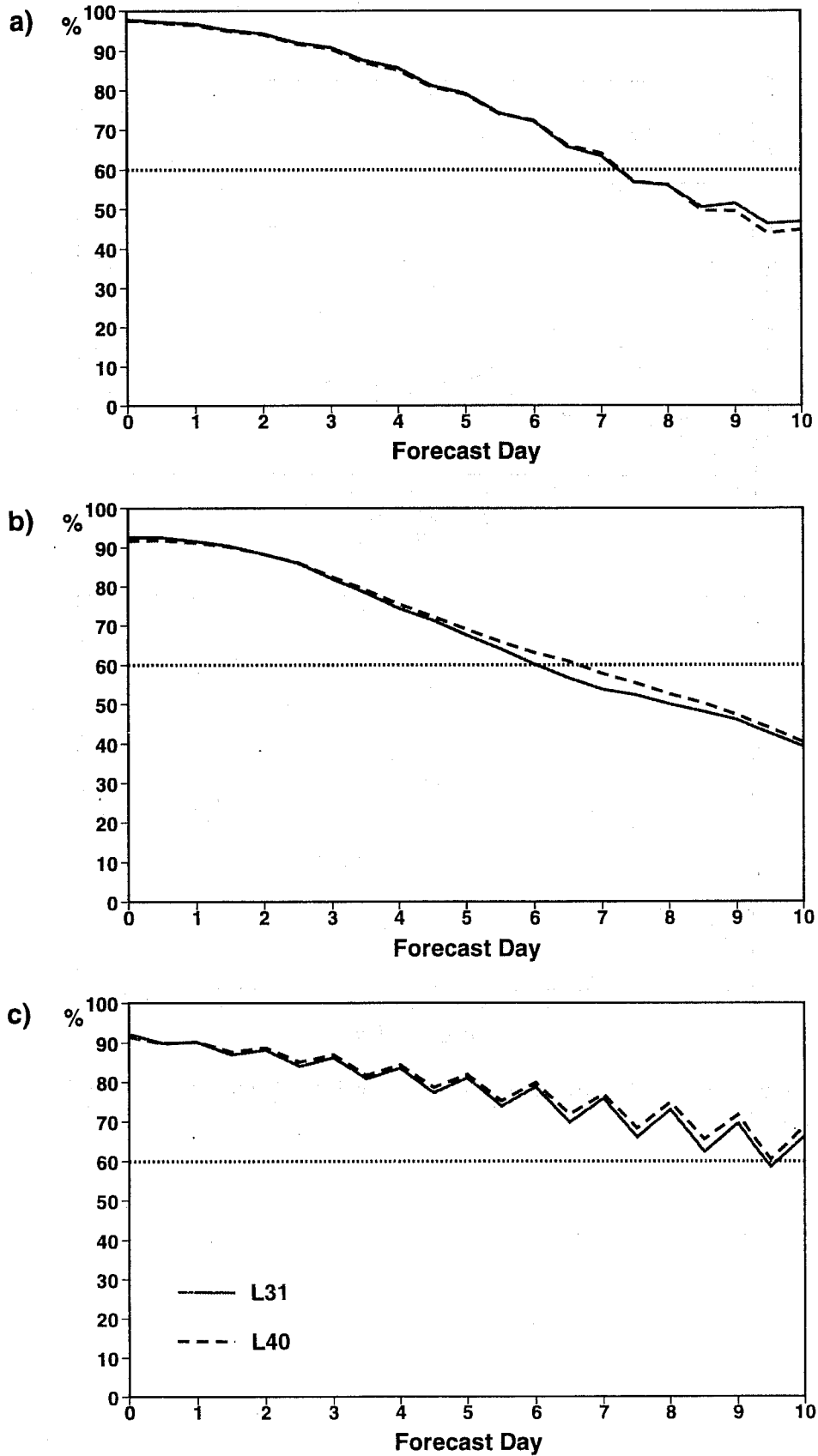
Fig. 32 The anomaly correlation for 17 spring 850 hPa temperature forecasts, for (a) the Northern and (b) Southern Hemisphere and (c) the Tropics.
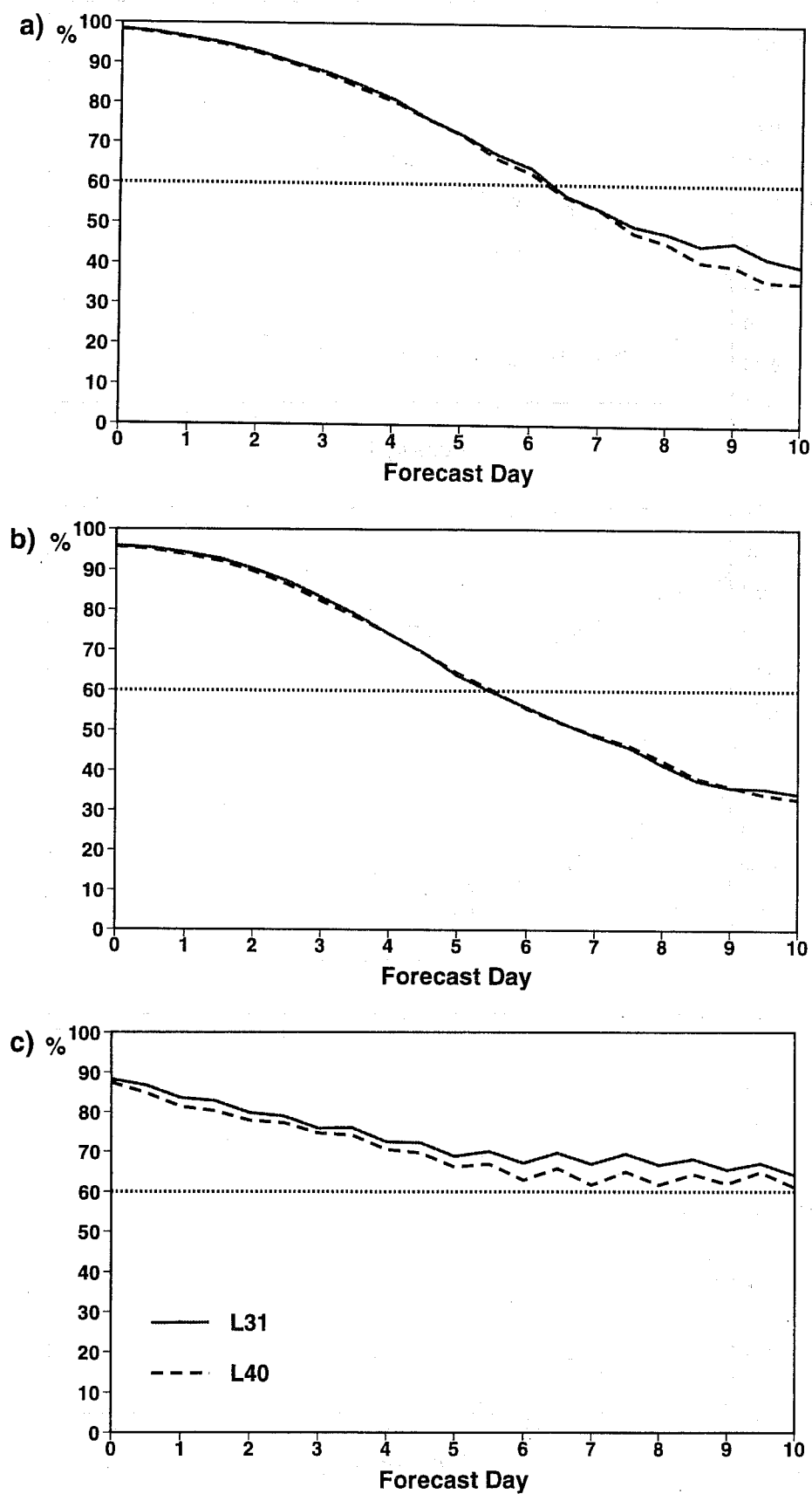
Fig. 34 The anomaly correlation scores for the 200 hPa temperature for the 17 spring forecasts for (a) the Northern
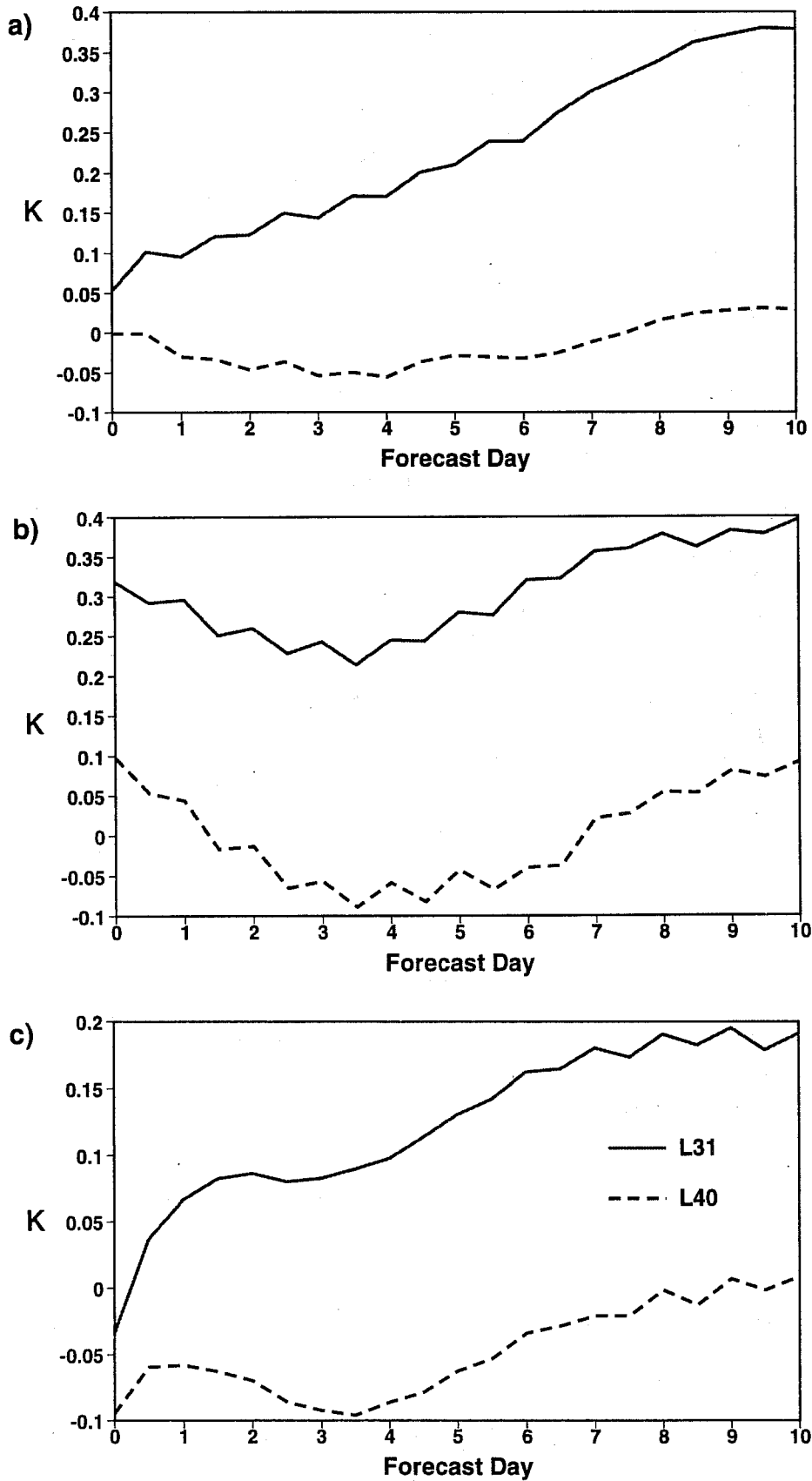and (b) Southern Hemisphere and (c) the Tropics.

Fig. 33 The mean 850 hPa temperature error of the 35 (winter and spring) forecasts, for (a) the Northern and (b) Southern Hemisphere and (c) the Tropics.
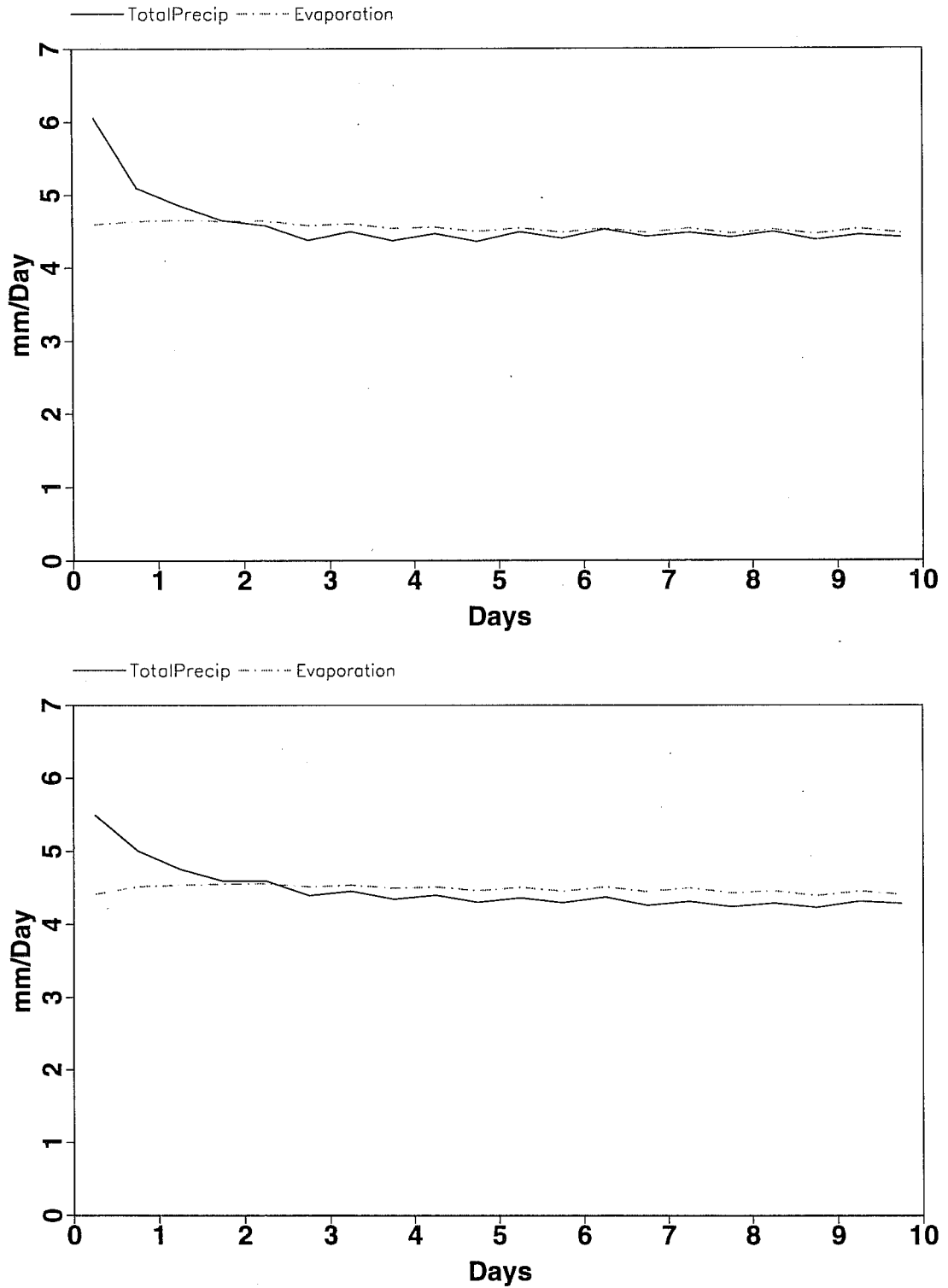
Fig. 35 Total precipitation and evaporation (mm/day) over the Tropics from (a) the L31 forecasts and (b) the L40 model.